Crystallographic preferred orientation, magnetic and seismic anisotropy in rocks from the Finero peridotite, Ivrea-Verbano zone, Northern Italy – interplay of anisotropy contributions from different minerals

Andrea R. Biedermann [1,2], Karsten Kunze[3,4], Alba S. Zappone[4,5]

[1] Institute of Geological Sciences, University of Bern, Baltzerstrasse 1+3, 3012 Bern, Switzerland

[2] Institute of Geophysics, ETH Zurich, Sonneggstrasse 5, 8092 Zurich, Switzerland

[3] Scientific Center for Optical and Electron Microscopy (ScopeM), Otto-Stern-Weg 3, 8093 Zurich, Switzerland

[4] Institute of Geology, ETH Zurich, Sonneggstrasse 5, 8092 Zurich, Switzerland

[5] Institute of Process Engineering, ETH Zurich, Sonneggstrasse 3, 8092 Zurich, Switzerland

Address for correspondence

Prof. Andrea R. Biedermann
Institute of Geological Sciences
University of Bern
Baltzerstrasse 1+3
3012 Bern
Switzerland
andrea.regina.biedermann@gmail.com
Phone: +41 (0)31 631 4534

The final version of this manuscript is available on the Tectonophysics website:

https://www.sciencedirect.com/science/article/abs/pii/S0040195120301074?via%3Dihub

DOI: 10.1016/j.tecto.2020.228424

Abstract

Mineral alignment can provide valuable information on a rock's geological history. Many structural, tectonic, or geodynamic studies rely on determining the preferred orientation of rock-forming minerals, either by direct texture determination or using anisotropy measurements as proxies. Robust interpretations of anisotropy require detailed understanding of its relationship with texture. This study investigates the texture, magnetic and seismic anisotropies of ultramafic rocks from the Ivrea-Verbano Zone (IVZ), Northern Italy, with a special focus on the interplay between anisotropy contributions carried by different minerals. Texture was obtained from electron backscatter diffraction, magnetic anisotropy from low- and high-field anisotropy of susceptibility measurements, and seismic anisotropy from P- and S-wave velocities along the three principal directions of the macroscopic fabric, using 22 mm diameter cores. Texture-based models of magnetic anisotropy agree well with corresponding measurements. Larger variability is observed for seismic anisotropy. Possible explanations are (1) velocities were measured in three directions, insufficient to determine the full elasticity tensor, and (2) seismic anisotropy depends on grain boundaries, pores, and cracks in addition to crystallographic preferred orientation. The contributions to magnetic and seismic anisotropy of each constituent mineral can interfere positively, leading to a larger overall anisotropy, or negatively, resulting in a weaker anisotropy. Seismic anisotropy is mostly controlled by olivine, whereas magnetic anisotropy can be dominated by olivine, pyroxene, or hornblende. This study illustrates that, although the relationship between texture and anisotropy can be complex, it is possible to quantitatively predict magnetic, and to a lesser degree seismic, anisotropy from texture data. Even though both magnetic and seismic anisotropies are common proxies for texture, they are not coaxial, and no simple relationship between the degree of magnetic and seismic anisotropy was found. These results underline the importance of understanding different minerals' contributions to anisotropy in upper mantle rocks.

Keywords: magnetic anisotropy, seismic anisotropy, EBSD, CPO, Ivrea-Verbano Zone, Finero peridotite, olivine, hornblende, phlogopite

1. Introduction

Crystallographic preferred orientation (CPO) of minerals arises during deformation of rocks, and thus provides information on geodynamic and tectonic processes. When the intrinsic physical properties of a mineral are anisotropic, and it possesses a CPO, it can contribute to anisotropy of bulk rock properties. Anisotropy and CPO are directly related for properties that depend on the bulk properties of a grain, rather than the grain boundaries (Mainprice et al., 2011; Mainprice and Humbert, 1994). Correlations between anisotropy and CPO have been described for example for thermal conductivity and diffusivity, magnetic susceptibility or seismic velocities (Gibert and Mainprice, 2009; Hess, 1964; Khazanehdari et al., 1998; Owens and Bamford, 1976; Owens and Rutter, 1978; Nicolas and Christensen, 1987; Tommasi et al., 2001).

Because anisotropy is a direct consequence of CPO, it often serves as proxy for rock texture. An advantage of anisotropy is that it can be characterized more efficiently than CPO. Additionally, a larger volume of grains can be targeted (Engler and Randle, 2009). For this reason, the anisotropies of magnetic susceptibility (AMS) or remanence (AMR), referred to as magnetic fabrics, are often used to determine flow directions or strain patterns (Borradaile and Henry, 1997; Borradaile and Jackson, 2010; Hrouda, 1982; Jackson and Tauxe, 1991; Jackson, 1991). Early magnetic fabric studies relied on qualitative and empirical relationships between magnetic and mineral fabrics, postulating that (1) the maximum susceptibility indicates lineation and minimum susceptibility is normal to foliation, and (2) the degree of anisotropy increases with increasing strain (Balsley and Buddington, 1960; Hirt et al., 1993; Kligfield et al., 1981). Later studies found correlations between magnetic fabrics and CPO or shape preferred orientation (SPO) of specific minerals (Chadima et al., 2004; Grégoire et al., 1998; Lüneburg et al., 1999; Siegesmund et al., 1995). After the magnetic properties of single crystals have been systematically characterized (Biedermann, 2018, and references therein), it is now possible to model magnetic anisotropy based on CPO data. These models allow to investigate which mineral dominates the anisotropy, and how the anisotropies of different minerals in a rock interfere with one another (Biedermann et al., 2018; Biedermann et al., 2015b; Kuehn et al., 2019; Schmidt et al., 2009).

Another advantage is that anisotropy measurements can be obtained for regions in the Earth where no direct texture measurements are possible. For example, seismic anisotropy in the mantle, as observed by shear wave splitting, provides information on mantle flow patterns (Silver, 1996; Silver and Chan, 1988; Vauchez and Barruol, 1996). The relationship between CPO and elastic properties of the upper mantle has been well established over the last 50 years (Babuška, 1972; Babuška and Cara, 1991; Carter et al., 1972; Nicolas and Christensen, 1987). Additionally, the link between seismic anisotropy, CPO, deformation mechanisms and stress fields has been investigated extensively for the lower crystalline continental crust (Burlini and Fountain, 1993; Lloyd et al., 2009; Tatham et al., 2008), and sedimentary rocks (Maddock, 2006; Valcke et al., 2006; Wenk et al., 2008). Nicolas and Christensen (1987) observed that olivine CPO forms through crystal reorientation during dislocation creep-dominated deformation in the upper mantle. Because the deformation regime has an effect on the olivine CPO observed in continental deformation zones (Tommasi et al., 1999), seismic anisotropy may carry information on the deformation regimes active in the lithospheric mantle. Modeling seismic anisotropy is much more common than similar magnetic models (Almqvist and Mainprice, 2017, and references therein). Some seismic modeling studies have employed AMS data for an initial fabric characterization, to define appropriate measurement directions for seismic measurements (Gaudreau et al., 2017; Punturo et al., 2017; Schmitt et al., 2007). However, even when CPO data were available for these studies, no attempts had been made to model the magnetic anisotropy.

Both seismic and magnetic anisotropy are related to the preferred alignment of a rock's constituent minerals. In addition, factors such as porosity, compositional banding, grain boundaries, microcracks, fractures and melt inclusions affect the seismic anisotropy (e.g. Babuška, 1984; Kern and Wenk 1990; Nur and Simmons, 1969; Siegesmund et al., 1991; Wendt et al., 2003).

The exact relationship between mineral alignment and anisotropy may be different for magnetic and seismic properties, because each property is defined by different characteristics of a mineral. On the single crystal scale, elastic anisotropy depends on the atomic distance and stiffness of chemical bonds between atoms in each direction. Conversely, magnetic anisotropy is predominantly controlled by the site occupancy, arrangement, and oxidation state of iron atoms in the crystal. As a consequence of their different origins, it is likely that the magnetic and seismic anisotropies of a rock are controlled by different minerals. For example, relatively small amounts of mafic minerals can completely dominate the magnetic anisotropy (Biedermann et al., 2016), whereas the seismic properties are likely dominated by the most abundant mineral (Almqvist and Mainprice, 2017). Additionally, magnetic properties are described by 2nd order tensors, but elasticity, which defines seismic anisotropy, is a tensor of 4th order. Hence, even though both types of physical anisotropies are used to describe texture, they do not necessarily carry the same information. Nevertheless, both types of anisotropy are used to infer texture, and it is interesting to establish correlations between their principal directions or degrees of anisotropy.

One challenge when interpreting anisotropies of multiphase aggregates, including rocks, is that the contributions to anisotropy carried by different mineral phases are not always coaxial. Biedermann et al. (2015b) and Kuehn et al. (2019) have observed both positive and negative interferences between magnetic anisotropy components related to different phases. Hence, the orientations of maximum, intermediate and minimum susceptibilities, respectively, can be sub-parallel for several anisotropy components, so that the overall anisotropy is enhanced. Conversely, the minimum susceptibility of one phase may be sub-parallel to the maximum susceptibility of another phase, so that the two components partially cancel each other, resulting in a weak overall anisotropy. Similarly, Michibayashi et al. (2016) suggested that destructive interferences between the P-wave anisotropies of different minerals may be responsible for the observed weak seismic anisotropy in a shear zone in slow-spreading oceanic crust of the Philippine Sea.

This study investigates the CPO, magnetic and seismic anisotropy of samples from the Finero peridotite (Ivrea-Verbano Zone, Northern Italy). The study particularly focuses on (1) how different minerals and their CPOs interact to define the overall anisotropy of the rock, (2) the influence that hydrous minerals such as phlogopite or hornblende may have on the bulk rock anisotropy, and (3) if there is any quantitative correlation between magnetic and seismic anisotropy, either in terms of principal directions or anisotropy degree. Correlations between CPO and magnetic/seismic anisotropies will be investigated based on measurements and models. The latter makes it possible to disentangle the contributions of individual minerals to the bulk rock anisotropy. The results presented here will help to better understand how anisotropy is related to CPO, and thus lead to more robust interpretations for tectonic and geodynamic studies employing anisotropy as a proxy for texture.

2. Geological setting

The samples characterized in this study are peridotites from the Finero Ultramafic Complex, located within the Ivrea-Verbano Zone (IVZ) in the Western Italian Alps. Because of its easy accessibility, excellent exposure, and the absence of pervasive retrograde metamorphism, the IVZ is one of the most studied lower-crustal transects worldwide. Even though the interpretation of the IVZ and adjacent Serie dei Laghi as a middle- to lower-continental crust have been recently criticized (Boriani et al., 2016 and references therein), it is commonly used as a model to help interpret features of deep crustal seismic profiles (Fountain, 1976; Holliger et al., 1994; Holliger et al., 1993; Khazanehdari et al., 2000; Rudnick and Fountain, 1995; Rutter et al., 1999; Tommasi et al., 2017). Only a few main aspects of the IVZ that are relevant to our study will be mentioned here, well aware that the papers we mention represent just a fraction of the significant existing literature.

The IVZ mainly consists of a metamorphosed volcano-sedimentary sequence, referred to as the Kinzigite Formation, and gabbroic to dioritic intrusive rocks, referred to as the Mafic Complex (Figure 1). The metamorphic grade in the IVZ increases towards the northwest, from upper amphibolite facies adjacent to the Serie dei Laghi, to granulite facies near the northwestern boundary of the IVZ at the Canavese Line tectonic lineament, which separates the IVZ from the Alpine terranes, here represented by the Sesia Zone (Peyronel Pagliani and Boriani, 1967; Schmid, 1967; Zingg, 1983). Metamorphosed shales and greywacke (the so-called kinzigites and stronalites), with minor quartzites and meta-carbonates, are interlayered with diorites, norites, and metabasites whose abundances gradually change from the southern part (metabasite predominant) to the northermost part (meta-sediments predominant). Mantle peridotite lenses, tectonically interfingered with the metasedimentary rocks (Quick et al., 1995), occur in the northern and western part of the IVZ, near the Canavese Line. The largest of these ultramafic lenses is the Finero peridotite, also called Finero Ultramafic Complex; it lies at the northern tip of the IVZ and consists of a peridotitic slice, enveloped into an intrusive magmatic sequence of mafic and ultramafic rocks. The main peridotite body is harzburgite, locally grading into dunite with layers of chromitite; thin dykes of pyroxenite (websterite) sharply cut the peridotite. The

Finero peridotite is characterized by the presence of hydrated minerals (pargasitic to edenitic amphibole and phlogopite) and it is anomalously enriched in minor and trace incompatible elements. These features have been interpreted as a testimony of a later re-fertilization of a primary restitic mantle (e.g. Coltorti and Siena, 1994; Lensch, 1968; Rutter et al., 2007). According to Zanetti et al. (1999) the metasomatic harzburgite contains up to 5 % and 25% of phlogopite and amphibole, respectively. Phlogopite and amphibole are also found in the pyroxenitic dykes. Early calculations based on sapphirine bearing layers between amphibole-lherzolite and garnetiferous metagabbro suggest conditions of crystallization of 900°C-950°C and 9±1 kbar (0.9±0.1 GPa) (Sills et al., 1983). The Finero peridotite therefore provides a unique opportunity to study seismic and magnetic anisotropy of metasomatic mantle and obtain information on the seismic and magnetic signature of hydrous phases in lower crustal conditions.

3. Sample description and methods

3.1 Sample petrography and microstructures

The Finero peridotite was chosen for this study for two reasons: (1) Its low degree of serpentinization makes it possible to study the relationships between texture and anisotropy of physical properties in fresh samples, without the need to account for alteration and secondary minerals. (2) Its reported variability in modal composition, especially with respect to hydrous minerals, allows to study the interplay of anisotropy contributions carried by different minerals. Seven peridotite block samples from the Finero Ultramafic Complex with different modal compositions were selected for this study (Figure 1). Optical microscopy observations on thin sections (30µm in thickness) ensured that the abundance of secondary minerals (serpentine in particular) was small, and that the samples were representative of the hydrous mineral content within the Finero peridotite. Samples ZAP201, ZAP202, ZAP204, and ZAP207 are spinel bearing harzburgites, and ZAP205 a spinel lherzolite, with phlogopite modal content, as determined from optical microscopy, from 0 to 8 %. Sample ZAP208 tends towards a more dunitic composition. Sample ZAP214 is a harzburgite, but differs from the other harzburgites by its high amphibole content (20%, determined by optical microscopy).

Optical microscopy analyses of thin sections show that the spinel-bearing harzburgites and the lherzolite are characterized by large olivine crystals, with average grain sizes of 1.5 mm (ZAP207) to 2.5 mm (ZAP202). The dunite sample ZAP208 is coarser and displays 3.5 mm average grain size. The amphibole-rich harzburgite ZAP214 possesses the smallest olivine grains (< 1.5 mm on average). In the harzburgites, the olivine grains generally display a shape preferred orientation, which helps define the pervasive foliation of the rocks. In the dunite, olivine displays more polygonal, equiaxial shapes. In all samples, olivine possesses intra-granular deformation features such as undulose extinction and subgrain boundaries. Those are especially prominent in ZAP202 and ZAP205 (Figure 2).

Orthopyroxene (enstatite) occurs in the harzburgites as dispersed interstitial grains with irregular shape and pinnacle terminations at the boundary with olivine (cf the enstatite grains in samples ZAP202 and ZAP205 shown in Figure 2). Grain size varies from a few microns, e.g. in the bands around coarse olivine grains of sample ZAP204, to a few millimeters, e.g. in ZAP201.

Clinopyroxenes (diopside) are minor constituents of harzburgites. Clinopyroxene crystals are dispersed, with irregular interstitial shapes and variable grain sizes. They are in general smaller than olivine and orthopyroxene.

Amphibole is dispersed through the harzburgite, but may concentrate locally in elongated lenses or layers. The crystals tend to be flattened in the foliation plane and slightly elongated parallel to the lineation. Their longest axis is up to 2mm long.

Phlogopite occurs as flakes with grain sizes up to 4-5 mm, and flattened in the foliation plane. The phlogopite crystals often display kinks (cf ZAP207 in Figure 2). Pinning of olivine grain boundaries at the contact with phlogopite crystals is observed in all samples.

The microstructure of ZAP214 corresponds to the protomylonites described in Tommasi et al. (2017). Large elongated olivine crystals are surrounded by a fine-grained matrix in a core and mantle structure (cf ZAP214 a and b in Figure 2). The olivine crystals show subgrain boundaries at high angles to their elongation (Figure 2, ZAP214b) The fine-grained matrix around the large crystals has been interpreted as the results of a dynamic recrystallization of olivine through bulging and subgrain rotation (Tommasi et al., 2017). The area fraction of recrystallized grains in ZAP214 amounts up to 15%. The fine-grained matrix is locally also composed of small interstitial crystals of clino- and orthopyroxene. Pyroxene porphyroclasts have irregular shapes and highly indented grain boundaries. Hornblende is particularly abundant in ZAP214, and shows undulose extinction but no recrystallization (Figure 2, ZAP214a).

Table 1 summarizes the modal compositions obtained from optical microscopy and scanning electron microscopy (SEM) data (electron backscatter diffraction, EBSD, and energy-dispersive X-ray spectroscopy, EDS). Note that ZAP208 was too coarse-grained to provide statistically significant results from SEM analysis. For all other samples, both methods result in similar estimates of olivine content. However, the concentrations of other minerals can vary. In particular, phlogopite content determined from the SEM (EDS and EBSD) data is significantly lower than estimated from optical microscopy. This discrepancy may be explained by any of the following: (1) Due to its platy habit and dark color, phlogopite's concentration may be overestimated in optical microscopy when it is oriented at a small angle to the plane of the section, whereas the SEM only sees the intersection of phlogopite and sample surface; (2) not all grains could be indexed, and because micas do not polish well, phlogopite may contribute disproportionally to the non-indexed portion of EBSD data; and (3) different sub-specimens were used for thin sections and EBSD scans, and the phlogopite distribution in the rock may be inhomogenous.

3.2 Sample preparation

Three mutually perpendicular cores of 22 mm diameter and 30 – 50 mm length were drilled from each peridotite block. The macroscopic foliation and lineation were used as reference frame; however, the macroscopic fabric of these massive peridotites is poorly defined. Foliation and lineation, respectively, are defined by the planar distribution of phlogopite and the elongation direction of hornblende and pyroxene, as well as the shape preferred orientation of olivine. The three cores were labeled x, y and z, based on the drilling direction; x indicates core axis parallel to lineation, z core axis normal to foliation, and y refers to core axis within the foliation plane and perpendicular to lineation. Seismic velocity, magnetic susceptibility and CPO were measured on the same cores. Because seismic velocity measurements require longer cores (3 to 4 cm) than AMS measurements (length/diameter ratio of 0.92), the seismic cores were subsampled prior to magnetic experiments. EBSD scans were performed on one core of every site. The ends cut from the cores were used to obtain thin sections for petrographic description.

3.3 Crystallographic preferred orientation

After the anisotropy measurements were completed, the surface of one core from each site was polished and lapped with silica gel for EBSD measurements. These were performed on a an EOscanTescan Vega-3 scanning electron microscope (SEM) (Tescan, Brno CZ), at the Scientific Center for Optical and Electron Microscopy (ScopeM) at ETH Zurich. The microscope is equipped with a Pegasus EBSD and EDS system (OIM, Orientation Imaging Microscopy, version 6.2) by Ametek-Edax (Mahway, NJ, USA), and was operated at a beam current of 3-5 nA and 20 kV acceleration voltage. The EBSD band positions and the EDS counts were simultaneously recorded during the acquisition scans. Only one phase was indexed during data acquisition, and all relevant mineral phases were indexed during post-processing. For this the OIM ChiScan routine was used in combination with user-defined windows defining the possible minerals from the EDS counts. The maps covered an area as large as possible on the 22 mm diameter cores, i.e. about 300 mm^2, with a step size of 20 µm, and were collected by comboscans using beam scanning and field-wide stage motion.

Crystallographic preferred orientation was computed from all indexed points on the regularly spaced grid. This allows to weight the individual mineral and orientation distribution by area, and is therefore better suited to calculate physical properties and their anisotropy than CPOs calculated based on one point per grain. The latter would overestimate the contribution of small grains, and underestimate the contribution of large grains. To be consistent, all CPOs shown in this manuscript and supplementary files are based on an equally spaced grid.

3.4 Magnetic measurements

Magnetic measurements included acquisition of isothermal remanent magnetization (IRM), to characterize the ferromagnetic minerals, and determination of AMS in low and high fields. High field AMS measurements have the advantage that the sub-fabric carried by paramagnetic minerals (i.e., olivine, phlogopite, pyroxene, amphibole) can be isolated from that of the ferromagnetic grains (e.g. magnetite). This is important because magnetite may dominate the susceptibility, but is largely irrelevant for describing the alignment of the rock-forming minerals. All magnetic experiments were performed at the Laboratory of Natural Magnetism, ETH Zurich.

3.4.1 Characterization of ferromagnetic inclusions

IRM acquisition was measured to characterize ferromagnetic inclusions, and to determine their saturation fields (if saturated, ferromagnetic contributions can be removed from high-field AMS measurements). Cores were initially magnetized at 2 T along the -Z direction with an ASC Scientific pulse magnetizer, followed by remagnetization along +Z in increasing fields between 20 mT and 2 T. Magnetization was measured after each step using a 2G 3-axis magnetometer. The remanent coercivity and saturation field obtained from these measurements are characteristic for a specific mineral and the saturation magnetization indicates mineral type as well as concentration.

3.4.2 Magnetic anisotropy

AMS was measured in low and high magnetic fields. Low-field measurements were conducted on an Agico (Brno, Czech Republic) MFK1-FA susceptibility bridge operated at a field of 200 A/m and a frequency of 976 Hz. The susceptibility tensor was computed based on 15 directional susceptibility measurements (Jelinek, 1977). The eigenvalues of this tensor, $k_1 \geq k_2 \geq k_3$, define the principal susceptibilities, and the corresponding eigenvectors are referred to as princicpal susceptibility directions. If susceptibility is represented by a magnitude ellipsoid, its shape can be described by $U = (2k_2 - k_1 - k_3)/(k_1 - k_3)$. The degree of anisotropy can be described by $k' = \sqrt{((k_1 - k)^2 + (k_2 - k)^2 + (k_3 - k)^2)/3}$, or alternatively by $P = k_1/k_3$. The mean susceptibility k is defined as $k = (k_1 + k_2 + k_3)/3$ (Jelinek, 1981, 1984). The susceptibility tensor determined with low-field methods is a superposition of the susceptibilities carried by diamagnetic, paramagnetic and ferromagnetic minerals.

High-field anisotropy was measured in order to separate paramagnetic and ferromagnetic components, based on the method described in Martín-Hernández and Hirt (2001). Measurements were performed on a torque magnetometer in six fields between 1.0 and 1.5 T, both at room temperature and at 77 K to enhance the paramagnetic contribution. Deviatoric susceptibility tensors are obtained for each component, and the degree and shape of the susceptibility ellipsoid are described by k' and U.

3.5 Density and seismic velocity measurements

Both sides of the cores were polished until parallel within 0.02 mm, and oven dried for at least 24 hours at 80°C prior to density and seismic measurements. Measurements were carried out at the Rock Deformation Laboratory at ETH Zurich.

3.5.1 Density measurements

Bulk density (i.e., the density of the entire rock, including minerals and pores) was calculated by weighing the cores after dehydration with a highly precise balance ($\pm 5.0\times10^{-7}$ kg tolerance), and determining the bulk volume (i.e., the volume of the entire rock, including minerals and pores) of each core from measured length and diameter, using a caliper ($\pm 2\times10^{-5}$m accuracy). The grain density (i.e., the density of the grain fraction, also known as matrix density) was determined on a gas displacement He-pycnometer apparatus (Accupyc II 1340, Micromeritics), measuring the matrix volume (i.e. the volume of only the minerals, without the pores) of the cores at room conditions. The standard deviation of each measurement was lower than 5%. The effective porosity was then calculated as the difference between grain and bulk density.

3.5.2 Seismic velocities

The compressional (Vp) and shear (Vs) elastic wave velocities were measured using the pulse transmission technique (Birch, 1960) at room temperature (292-307K), and pressures up to 450 MPa using an internally heated gas medium apparatus equipped with a hybrid waveguide and embedded piezoelectric elements (PZT) to transmit and receive waveforms through the sample. Details of the experimental setup are reported in Tisato and Marelli (2013). The specimen lengths were measured before and after each experimental run to minimize errors introduced by changes in sample size. All velocity measurements were made at a frequency of 1 MHz, and estimated error limits are ~0.7% for Vp, 1.5% for Vs, and 1 K for absolute temperature.

Velocity vs pressure data were fitted based on the four parameter equation proposed by Wepfer and Christensen (1991). Velocities were extrapolated to 0 pressure from the linear part of the velocity vs pressure plots (cf e.g. Burlini and Fountain, 1993). These fits for the P- and S-wave velocities of the x-, y-, and z-core for each sample were then used to calculate the seismic anisotropies, Avp and Avs respectively, defined as $A(\%) = \frac{v_{max}-v_{min}}{v_{mean}} * 100$ (Birch, 1960). Mean pressure derivatives have been calculated using best-fit solutions from the linear part of the velocity-pressure relation (150-450 MPa), and mean velocities at 0 MPa were obtained by extrapolation using the pressure derivatives.

3.5 Modeling of magnetic and seismic anisotropies

If a physical property of a rock depends on the properties of individual mineral grains rather than grain boundaries or fractures, it can be modeled based on a combination of (1) the single crystal physical properties of each mineral in the rock, and (2) their abundance and crystallographic preferred orientation (Mainprice et al., 2011; Mainprice and Humbert, 1994). The MATLAB toolbox MTex (Hielscher and Schaeben, 2008) was used to model both magnetic and seismic properties of the cores for which EBSD data was available. Single crystal susceptibility tensors were calculated from data reported by Biedermann et al. (2014b) for olivine, Biedermann et al. (2015c) for enstatite and diopside, Biedermann et al. (2015a) for hornblende, and Biedermann et al. (2014a) for phlogopite. Note that physical properties of crystals need to include all the symmetry elements of the crystal itself (Neumann, 1885; Nye, 1957). For monoclinic minerals such as diopside, hornblende, and phlogopite, this symmetry constraint means that one of the principal axes of the susceptibility tensor must be aligned with the 2-fold symmetry axis [010]. No symmetry constraints apply to the position of the other two principal axes with respect to the crystal frame of monoclinic crystals. Incidentally, the other two principal axes for hornblende happen to be parallel to (100) and [001] (Biedermann et al., 2015a), as it would be required by the symmetry of orthorhombic crystals (e.g., olivine and enstatite). For phlogopite, the two larger eigenvalues do not notably differ (Biedermann et al., 2014a), resulting in a tensor with (pseudo-)rotational symmetry in the basal plane (001). Elasticity tensors for calculating compressional and shear wave velocities were obtained from Isaak et al. (1989) for olivine, Chai et al. (1997) for enstatite, Isaak et al. (2005) for diopside, and Brown and Abramson (2016, pargasitic amphibole No. 8) for hornblende. Note that the latter differs from the widely used tensor for amphiboles (Aleksandrov and Ryzhova, 1961), because the initial measurement was likely affected by open cleavage. For phlogopite, the tensor reported by Chheda et al. (2014) was used. The single crystal magnetic and seismic properties are shown in Figure 3.

Modal compositions and the CPO of each mineral were derived from EBSD data. Magnetic and seismic tensors were computed for (1) each mineral phase, and (2) the overall anisotropy, defined by a weighted combination of all relevant phases. Average property tensors can be calculated in three ways; Voigt, Reuss and Hill averages, where the latter is the arithmetic mean of the former two (Hill, 1952; Reuss, 1929; Voigt, 1887, 1928). For elastic properties, Hill (1952) observed that the Hill average agrees best with measured values. Therefore, Hill averages were used here to compute the averaged seismic tensors. Conversely, because magnetic susceptibility can vary over several orders of magnitude between different minerals, Reuss and Hill averages may result in unrealistic mean susceptibility values. Therefore, Voigt averages were used to compute the total magnetic anisotropy. The contribution of magnetite and other low-abundance phases was not taken into account for the modeling.

4. Results

4.1 CPO

Due to the large grain sizes in comparison to the total EBSD scan area, the significance of the CPO data is limited by counting statistics in the rather small grain populations. Olivine posseses a weak CPO, where the [001] directions are grouped within the foliation plane, and normal to lineation in most samples. The crystallographic [100] directions can be sub-parallel to macroscopic lineation (ZAP204 and ZAP205), normal to foliation (ZAP214), or at an angle to lineation in a plane defined by the lineation and the pole to foliation (ZAP201, ZAP202) (Supplementary Figures A-F). Enstatite shows girdle distributions of [001] in the foliation plane for all samples except ZAP214. The latter displays a maximum of [001] axes normal to the foliation plane, while most samples display a grouping of [100] normal to the foliation plane. The CPO of diopside shows several strong maxima, because only a small number of individual diopside grains have been measured. Therefore, the statistical significance of the diopside CPO is questionable, and will not be discussed further. With the exception of ZAP214, the hornblende (100) poles are aligned with the pole of the foliation plane, and [001] directions form girdle distributions within the foliation plane, sometimes with a sub-maximum parallel to lineation. Phlogopite CPOs, similar to those of diopside, are sharp but not statistically relevant. It appears that the macroscopic foliation and lineation of all samples except ZAP214 correlate with the CPO of hornblende, and to a lesser degree enstatite. The hornblende and enstatite CPOs of ZAP214 seem at odds with the macroscopic texture, because their [001] directions are normal to the foliation plane, while hornblende (100) lies in the foliation plane. This means that the foliation and lineation indicated by the hornblende and enstatite CPO are not parallel to the macroscopic features of this sample, i.e. SPO, grain size and compositional banding.

4.2 Magnetic anisotropy

All samples possess significant magnetic anisotropy both in low and high magnetic fields. The principal susceptibility directions are consistent across cores of the same sample and orientation, and the degree and shape of anisotropy are similar for all specimens of the same sample. Low-field AMS results are summarized in Table A, Online Supplementary. Mean susceptibility varies from $2*10^{-7}$ m^3/kg to $1*10^{-5}$ m^3/kg, and is on the order of 10^{-7} m^3/kg for all samples except ZAP214. *P*-values are highest for samples ZAP207 and ZAP214 where $P \sim 1.2$, and vary between 1.05 and 1.10 for samples ZAP201, ZAP202, ZAP204, and ZAP205. Sample ZAP208 shows the largest variation, with *P* ranging from 1.05 to 1.39. The mean deviatoric susceptibility, k', is on the order of 10^{-9} m^3/kg to 10^{-8} m^3/kg for most samples, again with large variations in ZAP208. ZAP214 has the highest anisotropy degree, with k' around $8*10^{-7}$ m^3/kg. The shape parameter *U* varies between specimens, but is mostly prolate for samples of ZAP201, ZAP202, ZAP207, and ZAP214, and oblate for ZAP204 and ZAP205. For ZAP208, three specimens have prolate shapes and three have oblate shapes.

The large variation in mean susceptibilities is likely related to varying contributions of ferromagnetic minerals, which may also affect the low-field AMS. All samples acquire an IRM. The acquisition curves are similar for ZAP201, ZAP202, ZAP204, ZAP205, ZAP207, and ZAP208. Their IRM is saturated in fields of 200 – 300 mT. Sample ZAP214 has even lower coercivity, and saturates well below 100 mT (Figure 4a). These low coercivities and saturation fields indicate that the ferromagnetic signal is carried by magnetite, and the magnetite grains are larger in ZAP214 than the other samples. Additionally, the stronger saturation IRM, and higher susceptibility of ZAP214 compared to the other samples indicates a higher concentration of magnetite, which explains its larger mean susceptibility.

Paramagnetic and ferromagnetic contributions to the high-field AMS at both temperatures are summarized in Table B (Online Supplementary). At room temperature, the paramagnetic contribution is highest in sample ZAP205, where it contributes 76 % to 82 % of the high-field AMS signal. In ZAP201, ZAP202 and ZAP204, the paramagnetic contribution is 55 % - 75 %, in ZAP207 it varies between 40 % and 60 %, and in specimens from ZAP208 covers the entire range from 41 % to 86 %. Conversely, the paramagnetic component in ZAP214 is 10% and hence a minor part of the high-field AMS. At 77 K, the paramagnetic contribution is enhanced. The orientation of principal AMS axes is generally consistent for equally oriented cores and at both temperatures (Figure 4b-h). The paramagnetic *k′* at room temperature varies between $3*10^{-10}$ m^3/kg and $1*10^{-9}$ m^3/kg, except in ZAP214 where it is ca. $2*10^{-9}$ m^3/kg.

Comparing low- and high-field AMS reveals that the low-field principal directions are similar to those of the isolated ferromagnetic component at room temperature, suggesting that the low-field AMS is strongly dominated by the small fraction of ferromagnetic grains (Figure 4b-h). This highlights that only the isolated paramagnetic AMS should be compared to CPO, and that low-field AMS is likely inadequate to define the principal fabric directions.

4.3 Density and seismic anisotropy

Measured densities, P- and S-wave velocities are reported in Table 2. Bulk densities vary between 3.23 and 3.34 g/cm^3, and porosity is less than 0.22%. Figure 5 shows the experimental seismic data, reported as Vp and Vs versus confining pressure, together with the fitted curves, as well as computed anisotropy. The P-wave velocity extrapolated to 0 pressure, Vp0, varies between 7.47 km/s and 8.49 km/s, with anisotropies ranging from 1.76% to 7.58%. The S-wave velocities (Vs01 and Vs02) range from 4.36 km/s to 5.06 km/s.

4.4 Modeled magnetic and seismic anisotropy

CPO-based models of magnetic and seismic anisotropy indicate that each mineral contributes anisotropically to both magnetic and seismic properties of the Finero peridotites. The modelled whole-rock minimum susceptibility is normal to the macroscopic foliation in all samples except ZAP214, where the CPO and macroscopic features indicate different foliation and lineation orientations. The direction of the modelled maximum susceptibility is more variable. The modelled maximum and minimum P-wave velocities are sub-parallel to the macroscopic lineation and foliation, respectively, in most samples. Exceptions are ZAP201 and ZAP202 which display 45° rotations between modelled maximum and minimum velocities and macroscopic features, and ZAP214, where the modelled maximum P-wave velocity is normal to foliation, while the minimum velocity lies in the foliation plane.

The models illustrate the whole-rock anisotropies are complex composites of the contributions of individual minerals. The maximum and minimum directions of either property can be coaxial for several minerals in a sample, but often the directional variability of magnetic and seismic properties is distinct for each mineral contribution.

5. Discussion

5.1 Measured vs modeled anisotropy

Paramagnetic susceptibility, P- and S-wave velocities as modeled from the CPO data have been compared to the measurements in terms of principal or minimum and maximum directions, as well as anisotropy degree and shape (Figure 6-7, Table 3, online supplementary figures). Because the models allow separating the contributions of each mineral phase, the dominant carrier minerals for magnetic and seismic anisotropy, respectively, were also determined. Finally, the interplay of anisotropy contributions of different minerals was explored.

5.1.1 Agreement between measured and modeled anisotropies

Good agreement is observed between measured and modeled principal susceptibility directions, i.e., differences between model and measurement are generally smaller than the measured inter-specimen variation. The one exception to this general observation is ZAP207, where the k_1 and k_2 directions deviate about 45° between model and measurement, likely a consequence of the small difference between k_1 and k_2 principal susceptibilities.

Degree and shape of paramagnetic anisotropy agree for most sets of models and measurements, but not for all of them (Figure 8). A possible explanation for this is that the anisotropy degree strongly depends on iron content in single crystals, but due to the lack of chemical data, average single crystal tensors were used. Additionally, other minerals, e.g. serpentine, may contribute to the AMS, but were not considered in the models. Note that the CPOs of some minerals were not statistically relevant and may be unrepresentative. Also, sample heterogeneity may result in unrepresentative EBSD data, possibly resulting in discrepancies between models and measurements. Still, the generally good agreement between measured and modeled magnetic anisotropy indicates that the CPOs derived from the EBSD data, despite the statistical limitations described in Section 4.1, are sufficiently representative of the samples.

Larger variations are observed between measured and modeled maximum and minimum P-wave velocities. Note that the seismic data is not sufficient to calculate the full seismic tensor, and that the modeled maximum and minimum P-wave velocities are generally not parallel to the structural x-, y- and z-axes, along which seismic velocities were measured. When the three measurement directions do not include the true minimum and maximum velocities, the minimum measured velocity overestimates the true minimum velocity, and analogously, the maximum measured velocity underestimates the true maximum velocity. In this case, the seismic measurements underestimate the true elastic anisotropy. For this reason, seismic models and measurements cannot be directly compared in terms of principal directions, and the measured anisotropy is a lower threshold constraining the true seismic anisotropy. Instead, the velocities parallel to x, y and z, for which measurements are available, will be compared, and the measured maximum and minimum velocities are checked against the more complete velocity distribution provided by the models. Modeled and measured minimum P-wave velocities are consistent for samples ZAP205 and ZAP207, and the maximum velocities are consistent for ZAP202, ZAP204 and ZAP205. In ZAP201, model and measurement are oblique (Figure 7). The minimum measured P-wave velocity of ZAP214 is sub-parallel to the maximum modeled P-wave velocity, and vice versa. This apparent discrepancy in ZAP214 is likely related to the different orientations of CPO fabric as compared to the fabric of the macroscopic fabric features, namely shape preferred orientation and banding. Note that the models take into account exclusively CPO, whereas seismic measurements are affected by the microstructure in addition to CPO. The modeled velocities are almost always faster than those measured, and the modeled degree of anisotropy is generally lower than that measured (Figure 8). The latter is unexpected, given that the measurements represent a minimum estimate of seismic anisotropy. This indicates that factors other than CPO have a major influence on the seismic measurements, in that they reduce velocities and increase anisotropy. These may include microcracks and pores, grain boundaries, and additional minerals, such as serpentine.

5.1.2 Carrier minerals for magnetic and seismic anisotropies

Olivine is the main constituent of all samples, and largely controls their seismic anisotropy. The contributions of other minerals to seismic anisotropy are minor. Even for samples ZAP207 and ZAP214 that contain a relatively high percentage of hornblende, it appears that the orientation of minimum and maximum velocity is dominated by olivine. Particularly in ZAP214, the olivine and hornblende CPOs are such that the fast P-wave velocity in olivine [100] is sub-parallel to the fast axis of hornblende [001], so that their contributions interfere positively, leading to an overall stronger anisotropy.

The magnetic anisotropy is more complex, and can be dominated by olivine, pyroxene or hornblende, or a combination of all minerals. The magnetic tensor of ZAP204 is strongly influenced by enstatite and hornblende, and the minimum susceptibility of ZAP214 is controlled by hornblende. In most other samples, olivine has the strongest influence on the rock magnetic anisotropy. The magnetic tensors of olivine, hornblende and enstatite can either be in constructive (ZAP205, ZAP207) or destructive (ZAP202, ZAP204) interference.

Seismic and magnetic anisotropies reflect the CPOs of different minerals, and may be dominated by different details of the orientation distribution of a given mineral. While seismic anisotropy is dominated by olivine, the most abundant mineral, magnetic anisotropy can be controlled by minerals that are less abundant. Single crystal seismic properties (e.g., mean velocity) are rather uniform for the different minerals composing these rocks, whereas magnetic susceptibility and its anisotropy can vary largely from one mineral to another. Enstatite and hornblende generally have a higher *k'* than olivine, and therefore contribute over-proportionally to the overall susceptibility anisotropy. Olivine's contribution to anisotropy is predominantly controlled by the grouping of [001] in the case of magnetic anisotropy, but by the orientation distribution of [100] for seismic properties. The fact that different crystallographic directions control magnetic and seismic anisotropy is related to the difference in single crystal properties: single crystal magnetic susceptibility in olivine is prolate, with the maximum susceptibility being parallel to [001], whereas the maximum P-wave velocity is parallel to [100]. This may be exploited to investigate the details of olivine orientation distributions in future studies.

5.2 Correlations between rock texture, magnetic and seismic anisotropy

Both modelled and measured minimum susceptibilities are normal to the macroscopic foliation plane in all samples except ZAP214, where the minimum susceptibility lies in the foliation plane and perpendicular to lineation. A large scatter in minimum directions is observed in ZAP204. The maximum susceptibility is always at an angle to macroscopic lineation, and often nearly perpendicular to lineation in the foliation plane.

The measured seismic P-wave velocity is smallest normal to foliation except in sample ZAP204 where the two velocities measured normal to lineation are very similar. The fastest P-wave velocity is observed parallel to lineation in all samples except ZAP207 and ZAP214 where it is observed in the foliation plane, but normal to lineation. Larger directional variability is observed in the models. Note that these peridotites are massive rocks, with poorly defined macroscopic foliation and lineation. Furthermore, lineation is defined by hornblende and pyroxenes, whereas the seismic P-wave anisotropy appears to be dominated by olivine. Nevertheless, the disagreement between the seismic models and measurements illustrates that CPO is not the only factor defining seismic anisotropy.

No straightforward relationship exists between the orientations of mineral fabric, magnetic and seismic anisotropies in these complex rocks, containing several constituent minerals contributing to their physical properties. Neither the principal susceptibility nor the minimum and maximum velocity directions necessarily coincide with the macroscopic foliation and lineation. This is observed both for magnetic anisotropy, which can be reliably modeled based on CPO, and for seismic anisotropy, where larger discrepancies are observed between model and measurement. The reason for this is that the macroscopic foliation and lineation are defined mainly by hornblende and mica (as well as serpentinization and grain size banding in ZAP214), whereas the seismic anisotropy is controlled by olivine, and the magnetic anisotropy is a complex fabric consisting of contributions from olivine, pyroxenes and hornblende in various proportions. A particularly important result of this study is that the maximum and minimum velocities and susceptibilities are generally not parallel to each other. This observation would advise against the use of AMS data to define the 3 measurement directions for seismic anisotropy measurements, and suggests that seismic anisotropy was underestimated in previous studies (Gaudreau et al., 2017; Punturo et al., 2017). Further, the results presented here highlight the need for more than 3 independent measurements of the elasticity tensor, e.g. based on the experimental method proposed by Mah and Schmitt (2001, 2003)

There is no clear correlation between the degree of magnetic and seismic anisotropy, again likely a result of the different carrier minerals (Figure 9). This is consistent with results by Schmitt et al. (2007) who found a decrease of the seismic anisotropy degree with increasing serpentinization, but no systematic correlation with magnetic anisotropy in ophiolite.

5.3 Influence of hydrous minerals on physical properties

The hydrous minerals, hornblende and phlogopite, influence the magnetic anisotropy of the peridotite rocks from the IVZ. Specifically, the principal susceptibility directions of ZAP207 and ZAP214 are controlled by hornblende CPO, and have different orientations than the anisotropy contribution of either olivine or enstatite. In samples where the anisotropy of hornblende interferes positively with that of olivine (ZAP201, ZAP205, ZAP207), the overall anisotropy is increased with respect to the olivine contribution alone. In samples ZAP202, ZAP204, and ZAP214, where the hornblende and olivine anisotropy interfere destructively, the overall anisotropy is diminished.

The influence of hydrous minerals on seismic anisotropy is smaller in that the minimum and maximum velocity directions are defined by the olivine contribution in all samples. The degree of anisotropy, on the other hand, is affected by the presence of hornblende. Similar to the magnetic properties, the contributions of olivine and hornblende can lead to a larger or smaller seismic anisotropy than the olivine contribution on its own. Positive interferences are observed in ZAP205, ZAP207, and partly ZAP214.

More work on different geological settings with different CPOs will be needed to establish a more detailed understanding of the relationship between texture and anisotropy of physical properties in general, and specifically the influence of certain mineral phases on these relationships.

6. Conclusions

Mineral texture has been compared to anisotropy of physical properties for a suite of rocks from the Finero peridotite in the IVZ. Whereas the minimum susceptibility of most samples is normal to their macroscopic foliation, there is often a large deviation between maximum susceptibility and lineation direction. CPO-based models of the magnetic anisotropy shows that (1) the paramagnetic anisotropy can be reliably modeled in terms of principal directions, and to a lesser extent in terms of anisotropy degree and shape, and (2) the main carrier minerals of the magnetic anisotropy can be olivine, pyroxene, or hornblende, or a combination thereof. Note that the contributions of these mineral groups can interfere positively or negatively, depending on the sample.

Seismic velocities measured along three directions often indicate the correct macroscopic lineation and foliation. However, CPO-based models of seismic anisotropy do not generally agree with these measurements. In particular, the modeled maximum and minimum velocity directions are generally not parallel to any of the structural directions. This suggests that more than three measurement directions are needed to fully capture the seismic anisotropy. Additionally, the discrepancy between measured and modeled seismic anisotropies illustrates that seismic properties are affected by factors other than CPO, such as microcracks and fractures, porosity, the number and alignment of grain boundaries.

Anisotropy measurements capture a volume and hence a larger number of grains than EBSD measurements obtained on a surface. Therefore, anisotropy measurements may be representative of the overall grain alignment in a sample on which direct texture determination is limited by poor counting statistics. Whereas our results clearly illustrate that magnetic anisotropy is not reliable at predicting the maximum and minimum velocity directions, magnetic anisotropy is a fast and efficient statistical tool to determine whether drill cores are representative of a larger sample. The agreement between modeled and measured magnetic anisotropy can also be used to support statistical relevance of the CPO of the phases dominantly carrying the magnetic anisotropy.

Because macroscopic fabric, magnetic and seismic anisotropy are predominantly defined by different carrier minerals, there is no straightforward relationship between them. The principal axes are in general not coaxial, and we did not observe any correlation between the magnetic and seismic degrees of anisotropy. Contributions of different minerals can interfere constructively or destructively, thus resulting in a larger or smaller overall anisotropy than the anisotropy of the dominant mineral alone. The results and models shown here, in particular the interplay between the anisotropies of different constituent mineral phases, allows a deeper understanding of physical anisotropy in complex, multi-phase aggregates. This detailed and profound understanding will help future interpretations of textures, and hence geodynamic processes, based on anisotropy data.

Acknowledgments

We are grateful to Remy Lüchinger for preparing thin sections. Ann Hirt and Hans-Peter Hächler are thanked for access to the Laboratory of Natural Magnetism, ETH Zurich, and help with the measurements. Access to the SEM-EBSD facility at the Laboratory for Nanometallurgy, ETH Zurich, through ScopeM is gratefully acknowledged. We also thank Xin Zhong for help with EBSD data, and Xin Zhong and Michaela Erni for performing initial seismic measurements at the Rock Deformation Laboratory, ETH Zurich. Magnetic measurements and modeling were supported by Swiss National Science Foundation project 143438.

References

Aleksandrov, K.S., Ryzhova, T.V., 1961. The elastic properties of rock-forming minerals: pyroxenes and amphiboles. Bull. USSR Acad. Sci. Geophys. Ser. 9, 871-875.

Almqvist, B.S.G., Mainprice, D., 2017. Seismic properties and anisotropy of the continental crust: Predictions based on mineral texture and rock microstructure. Reviews of Geophysics 55, 367-433.

Babuška, V., 1972. Elasticity and anisotropy of dunite and bronzitite. Journal of Geophysical Research 77, 6955-6965.

Babuška, V., 1984. P-wave velocity anisotropy in crystalline rocks. Geophysical Journal of the Royal Astronomical Society 76, 113-119.

Babuška, V., Cara, M., 1991. Seismic Anisotropy in the Earth. Springer Netherlands, p. 219.

Balsley, J.R., Buddington, A.F., 1960. Magnetic susceptibility anisotropy and fabric of some Adirondack granites and orthogneisses. American Journal of Science 258-A, 6-20.

Biedermann, A.R., 2018. Magnetic Anisotropy in Single Crystals: A Review. Geosciences 8.

Biedermann, A.R., Bender Koch, C., Lorenz, W.E.A., Hirt, A.M., 2014a. Low-temperature magnetic anisotropy in micas and chlorite. Tectonophysics 629, 63-74.

Biedermann, A.R., Bender Koch, C., Pettke, T., Hirt, A.M., 2015a. Magnetic anisotropy in natural amphibole crystals. American Mineralogist 100, 1940-1951.

Biedermann, A.R., Kunze, K., Hirt, A.M., 2018. Interpreting magnetic fabrics in amphibole-bearing rocks. Tectonophysics 722, 566-576.

Biedermann, A.R., Kunze, K., Zappone, A.S., Hirt, A.M., 2015b. Origin of magnetic fabric in ultramafic rocks. IOP Conference Series: Materials Science and Engineering 82.

Biedermann, A.R., Pettke, T., Angel, R.J., Hirt, A.M., 2016. Anisotropy of magnetic susceptibility in alkali feldspar and plagioclase. Geophysical Journal International 205, 479-489.

Biedermann, A.R., Pettke, T., Bender Koch, C., Hirt, A.M., 2015c. Magnetic anisotropy in clinopyroxene and orthopyroxene single crystals. Journal of Geophysical Research - Solid Earth 120, 1431-1451.

Biedermann, A.R., Pettke, T., Reusser, E., Hirt, A.M., 2014b. Anisotropy of magnetic susceptibility in natural olivine single crystals. Geochemistry Geophysics Geosystems 15, 3051-3065.

Birch, F., 1960. The velocity of compressional waves in rocks to 10 Kilobars, part 1. Journal of Geophysical Research 65, 1083-1102.

Boriani, A., Caironi, V., Sacchi, R., 2016. The CMB Line: the southern margin of the Ivrea–Verbano Zone (basement of Southern Alps, Italy): a re-appraisal. Rendiconti Lincei, 1-6.

Borradaile, G.J., Henry, B., 1997. Tectonic applications of magnetic susceptibility and its anisotropy. Earth-Science Reviews 42, 49-93.

Borradaile, G.J., Jackson, M., 2010. Structural geology, petrofabrics and magnetic fabrics (AMS, AARM, AIRM). Journal of Structural Geology 32, 1519-1551.

Brack, P., Ulmer, P., Schmid, S.M., 2010. A crustal-scale magmatic system from the Earth's mantle to the Permian surface – Field trip to the area of lower Valsesia and Val d'Ossola (Massiccio dei Laghi, Southern Alps, Northern Italy). Swiss Bulletin für angewandte Geologie 15, 3-21.

Brown, J.M., Abramson, E.H., 2016. Elasticity of calcium and calcium-sodium amphiboles. Physics of the Earth and Planetary Interiors 261, 161-171.

Burlini, L., Fountain, D.M., 1993. Seismic anisotropy of metapelites from the Ivrea-Verbano zone and Serie dei Laghi (northern Italy). Physics of the Earth and Planetary Interiors 78, 301-317.

Carter, N.L., Baker, D.W., George, R.P., 1972. Seismic Anisotropy, Flow, and Constitution of the Upper Mantle, in: Heard, H.C., Borg, I.Y., Carter, N.L., Raleigh, C.B. (Eds.), Flow and Fracture of Rocks. American Geophysical Union, Washington, D. C., pp. 167-190.

Chadima, M., Hansen, A., Hirt, A.M., Hrouda, F., Siemens, H., 2004. Phyllosilicate preferred orientation as a control of magnetic fabric: Evidence from neutron texture goniometry and low and high-field magnetic anisotropy (SE Rhenohercynian Zone of Bohemian Massif), in:

Martín-Hernández, F., Lüneburg, C.M., Aubourg, C., Jackson, M. (Eds.), Magnetic Fabric: Methods and Applications. The Geological Society, London UK, pp. 361-380.

Chai, M., Brown, J.M., Slutsky, L.J., Zang, J., 1997. The elastic constants of an aluminous orthopyroxene to 12.5 GPa. Journal of Geophysical Research 102, 14779-14785.

Chheda, T.D., Mookherjee, M., Mainprice, D., dos Santos, A.M., Molaison, J.J., Chantel, J., Manthilake, G., Bassett, W.A., 2014. Structure and elasticity of phlogopite under compression: Geophysical implications. Physics of the Earth and Planetary Interiors 233, 1-12.

Coltorti, M., Siena, F., 1994. Mantle tectonite and fractionate peridotite at Finero (Italian Western Alps). Neues Jahrbuch für Mineralogie 149, 225-244.

Engler, O., Randle, V., 2009. Introduction to Texture Analysis: Macrotexture, Microtexture, and Orientation Mapping. CRC Press, Boca Raton, US.

Fountain, D.M., 1976. The Ivrea—Verbano and Strona-Ceneri Zones, Northern Italy: A cross-section of the continental crust—New evidence from seismic velocities of rock samples. Tectonophysics 33, 145-165.

Gaudreau, E., Schneider, D., Lagroix, F., Cossette, E., Grasemann, B., 2017. Controls and implications of anisotropy across a strain gradient within granodiorite, Serifos, Greece. Journal of Geodynamics 105, 11-26.

Gibert, B., Mainprice, D., 2009. Effect of crystal preferred orientations on the thermal diffusivity of quartz polycrystalline aggregates at high temperature. Tectonophysics 465, 150-163.

Grégoire, V., Darrozes, P., Gaillot, P., Nédélec, A., 1998. Magnetite grain shape fabric and distribution anisotropy vs rock magnetic fabric: a three-dimensional case study. Journal of Structural Geology 20, 937-944.

Hefferan, K., O'Brien, J., 2010. Earth Materials. Wiley-Blackwell. 624pp.

Hess, H.H., 1964. Seismic anisotropy of the uppermost mantle under oceans. Nature 203, 629-631.

Hielscher, R., Schaeben, H., 2008. A novel pole figure inversion method: specification of the MTex algorithm. Journal of Applied Crystallography 41, 1024-1037.

Hill, R., 1952. The elastic behaviour of a crystalline aggregate. Proceedings of the Physical Society A 65, 349-354.

Hirt, A.M., Lowrie, W., Clendenen, W.S., Kligfield, R., 1993. Correlation of strain and the anisotropy of magnetic susceptibility in the Onaping Formation: evidence for a near-circular origin of the Sudbury Basin. Tectonophysics 225, 231-254.

Holliger, K., Levander, A., Carbonell, R., Hobbs, R., 1994. Some attributes of wavefields scattered from Ivrea-type lower crust. Tectonophysics 232, 267-279.

Holliger, K., Levander, A., Goff, J.A., 1993. Stochastic modeling of the reflective lower crust: Petrophysical and geological evidence from the Ivera Zone (northern Italy). Journal of Geophysical Research - Solid Earth 98, 11967-11980.

Hrouda, F., 1982. Magnetic anisotropy of rocks and its application in geology and geophysics. Geophysical Surveys 5, 37-82.

Isaak, D.G., Anderson, O.L., Goto, T., Suzuki, I., 1989. Elasticity of single-crystal forsterite measured to 1700 K. Journal of Geophysical Research 94, 5895-5906.

Isaak, D.G., Ohno, I., Lee, P.C., 2005. The elastic constants of monoclinic single-crystal chrome-diopside to 1,300 K. Physics and Chemistry of Minerals 32, 691-699.

Jackson, M., Tauxe, L., 1991. Anisotropy of magnetic susceptibility and remanence: Developments in the characterization of tectonic, sedimentary, and igneous fabric. Reviews of Geophysics 29, 371-376.

Jackson, M.J., 1991. Anisotropy of magnetic remanence: A brief review of mineralogical sources, physical origins, and geological applications, and comparison with susceptibility anisotropy. Pure and Applied Geophysics 136, 1-28.

Jelinek, V., 1977. The statistical theory of measuring anisotropy of magnetic susceptibility of rocks and its application.

Jelinek, V., 1981. Characterization of the magnetic fabric of rocks. Tectonophysics 79, T63-T67.

Jelinek, V., 1984. On a mixed quadratic invariant of the magnetic susceptibility tensor. Journal of Geophysics - Zeitschrift Fur Geophysik 56, 58-60.

Kern, H., Wenk, H.-R., 1990. Fabric-related velocity anisotropy and shear wave splitting in rocks from the Santa Rosa Mylonite Zone, California. Journal of Geophysical Research, 95(B7), 11213–11223.

Khazanehdari, J., Rutter, E.H., Brodie, K.H., 2000. High-pressure-high-temperature seismic velocity structure of the midcrustal and lower crustal rocks of the Ivrea-Verbano zone and Serie dei Laghi, NW Italy. Journal of Geophysical Research - Solid Earth 105, 13843-13858.

Khazanehdari, J., Rutter, E.H., Casey, M., Burlini, L., 1998. The role of crystallographic fabric in the generation of seismic anisotropy and reflectivity of high strain zones in calcite rocks. Journal of Structural Geology 20, 293-299.

Kligfield, R., Owens, W.H., Lowrie, W., 1981. Magnetic susceptibility anisotropy, strain, and progressive deformation in Permian sediments from the Maritime Alps (France). Earth and Planetary Science Letters 55, 181-189.

Kuehn, R., Hirt, A.M., Biedermann, A.R., Leiss, B., 2019. Quantitative comparison of microfabric and magnetic fabric in black shales from the Appalachian plateau (western Pennsylvania, U.S.A.). Tectonophysics 765, 161-171.

Lensch, G., 1968. Die Ultramafitite der Zone von Ivrea und ihre geologische Interpretation. Schweizerische mineralogische und petrographische Mitteilungen 48, 91-102.

Lloyd, G.E., Butler, R.W.H., Casey, M., Mainprice, D., 2009. Mica, deformation fabrics and the seismic properties of the continental crust. Earth and Planetary Science Letters 288, 320-328.

Lüneburg, C.M., Lampert, S.A., Lebit, H.D., Hirt, A.M., Casey, M., Lowrie, W., 1999. Magnetic anisotropy, rock fabrics and finite strain in deformed sediments of SW Sardinia (Italy). Tectonophysics 307, 51-74.

Maddock, J.S., 2006. Seismic anisotropy in siliciclastic reservoir rocks Faculty of Environment. University of Leeds., Leeds.

Mah, M., Schmitt, D.R., 2001. Experimental determination of the elastic coefficients of an orthorhombic material. Geophysics 66, 1217-1225.

Mah, M., Schmitt, D.R., 2003. Determination of the complete elastic stiffnesses from ultrasonic phase velocity measurements. Journal of Geophysical Research: Solid Earth 108, ECV 6-1-ECV 6-11.

Mainprice, D., Hielscher, R., Schaeben, H., 2011. Calculating anisotropic physical properties from texture data using the MTEX open-source package. Geological Society, London, Special Publications 360, 175-192.

Mainprice, D., Humbert, M., 1994. Methods of calculating petrophysical properties from lattice preferred orientation data. Surveys in Geophysics 15, 575-592.

Martín-Hernández, F., Hirt, A.M., 2001. Separation of ferrimagnetic and paramagnetic anisotropies using a high-field torsion magnetometer. Tectonophysics 337, 209-221.

Michibayashi, K., Watanabe, T., Harigane, Y., Ohara, Y., 2016. The effect of a hydrous phase on P-wave velocity anisotropy within a detachment shear zone in the slow-spreading oceanic crust: A case study from the Godzilla Megamullion, Philippine Sea. Island Arc 25, 209-219.

Neumann, F.E., 1885. Vorlesungen über die Theorie der Elastizität der festen Körper und des Lichtäthers, in: Meyer, O.E. (Ed.). B.G. Teubner Verlag, Leipzig, Germany.

Nicolas, A., Christensen, N.I., 1987. Formation of anisotropy in upper mantle peridotites: A review, in: Fuchs, K., Froidevaux, C. (Eds.), Composition, Structure and Dynamics of the Lithosphere-Asthenosphere System, Geodyn. Ser. AGU, Washington, D.C., pp. 111-123.

Nur, A., Simmons, G., 1969. The effect of saturation on velocity in low porosity rocks. Earth and Planetary Science Letters 7, 183-193.

Nye, J.F., 1957. Physical properties of crystals: Their representation by tensors and matrices. Clarendon Press, Oxford, UK.

Owens, W.H., Bamford, D., 1976. Magnetic, seismic, and other anisotropic properties of rock fabrics. Philosophical Transactions of the Royal Society A 283, 55-68.
Owens, W.H., Rutter, E.H., 1978. The development of magnetic susceptibility anisotropy through crystallographic preferred orientation in a calcite rock. Physics of the Earth and Planetary Interiors 16, 215-222.
Peyronel Pagliani, G., Boriani, A., 1967. Metamorfismo crescente nelle metamorfiti del «Massiccio dei Laghi» nella zona bassa Val d'Ossola – Verbania. Rend. Soc. Mineral. It. 23, 351-397.
Punturo, R., Mamtani, M.A., Fazio, E., Occhipinti, R., Renjith, A.R., Cirrincione, R., 2017. Seismic and magnetic susceptibility anisotropy of middle-lower continental crust: Insights for their potential relationship from a study of intrusive rocks from the Serre Massif (Calabria, southern Italy). Tectonophysics 712-713, 542-556.
Quick, J.E., Sinigoi, S., Mayer, A., 1995. Emplacement of mantle peridotite in the lower continental crust, Ivrea-Verbano Zone, northwest Italy. Geology 23, 739-742.
Reuss, A., 1929. Berechnung der Fliessgrenze von Mischkristallen auf Grund der Plastizitätsbedingung für Einkristalle. Zeitschrift für angewandte Physik 9, 49-58.
Rudnick, R.L., Fountain, D.M., 1995. Nature and composition of the continental crust: A lower crustal perspective. Reviews of Geophysics 33, 267-309.
Rutter, E.H., Brodie, K.H., James, T., Burlini, L., 2007. Large scale folding in the upper part of the Ivrea-Verbano zone. Journal of Structural Geology 29, 1-17.
Rutter, E.H., Khazanehdari, J., Brodie, K.H., Blundell, D., Waltham, D., 1999. Synthetic seismic reflection profile through the Ivrea-Verbano zone - Serie dei Laghi continental crustal section, northwestern Italy. Geology 27, 79-82.
Schmid, R., 1967. Zur Petrographie und Struktur der Zone Ivrea-Verbano zwischen Valle d'Ossola und Val Grande (Prov. Novara, Italien). Schweizerische Mineralogische und Petrographische Mitteilungen 47, 935-1117.
Schmidt, V., Hirt, A.M., Leiss, B., Burlini, L., Walter, J.M., 2009. Quantitative correlation of texture and magnetic anisotropy of compacted calcite–muscovite aggregates. Journal of Structural Geology 31, 1062-1073.
Schmitt, D.R., Han, Z., Kravchinsky, V.A., Escartin, J., 2007. Seismic and magnetic anisotropy of serpentinized ophiolite: Implications for oceanic spreading rate dependent anisotropy. Earth and Planetary Science Letters 261, 590-601.
Siegesmund S., Kern, H., Vollbrecht, A., 1991. The effect of oriented microcracks on seismic velocities in an ultramylonite, Tectonophysics 186, 241-251.
Siegesmund, S., Ullemeyer, K., Dahms, M., 1995. Control of magnetic rock fabrics by mica preferred orientation - a quantitative approach. Journal of Structural Geology 17, 1601-1613.
Sills, J.D., Ackermand, D., Herd, R.K., Windley, B.F., 1983. Bulk composition and mineral parageneses of sapphirine-bearing rocks along a gabbro-lherzolite contact at Finero, Ivrea Zone, N Italy. Journal of Metamorphic Geology 1, 337-351.
Silver, P.G., 1996. Seismic anisotropy beneath the continents: Probing the depths of geology. Annual Review of Earth and Planetary Sciences 24, 385-432.
Silver, P.G., Chan, W.W., 1988. Implications for continental structure and evolution from seismic anisotropy. Nature 335, 34-39.
Tatham, D.J., Lloyd, G.E., Butler, R.W.H., Casey, M., 2008. Amphibole and lower crustal seismic properties. Earth and Planetary Science Letters 267, 118-128.
Tisato, N., Marelli, S., 2013. Laboratory measurements of the longitudinal and transverse wave velocities of compacted bentonite as a function of water content, temperature, and confining pressure. Journal of Geophysical Research - Solid Earth 118, 3380-3393.
Tommasi, A., Tikoff, B., Vauchez, A., 1999. Upper mantle tectonics: three-dimensional deformation, olivine crystallographic fabrics and seismic properties. Earth and Planetary Science Letters 168, 173-186.

Tommasi, A., Gibert, B., Seipold, U., Mainprice D., 2001. Anisotropy of thermal diffusivity in the upper mantle. Nature 411, 783-786.

Tommasi A., Langone A., Padron-Navarta J. A., Zanetti A., 2017. Hydrous melts weaken the mantle, crystallization of pargasite and phlogopite does not: Insights from a petrostructural study of the Finero peridotites, southern Alps.Earth and Planetary Science Letters 477, 59–72.

Valcke, S.L.A., Casey, M., Lloyd, G.E., Kendall, J.-M., Fisher, Q.J., 2006. Lattice preferred orientation and seismic anisotropy in sedimentary rocks. Geophysical Journal International 166, 652-666.

Vauchez, A., Barruol, G., 1996. Shear-wave splitting in the Appalachians and the Pyrenees: importance of the inherited tectonic fabric of the lithosphere. Physics of the Earth and Planetary Interiors 95, 127-138.

Voigt, W., 1887. Theoretische Studien über die Elastizitätsverhältnisse. Abhandlungen der Akademie der Wissenschaften in Göttingen 34, 48-55.

Voigt, W., 1928. Lehrbuch der Kristallographie. Teubner-Verlag, Leipzig, Germany.

Wendt, A.S., Bayuk, I.O., Covey-Crump, S.J., Wirth, R., Lloyd, G.E., 2003. An experimental and numerical study of the microstructural parameters contributing to the seismic anisotropy of rocks. Journal of Geophysical Research - Solid Earth 108, 2365.

Wenk, H.-R., Voltolini, M., Mazurek, M., Van Loon, L.R., Vinsot, A., 2008. Preferred Orientations and Anisotropy an Shales: Callovo-Oxfordian Shale (France) and Opalinus Clay (Switzerland). Clays and Clay Minerals 56, 285–306.

Wepfer, W.W., Christensen, N.I., 1991. A seismic velocity-confining pressure relation, with applications. International Journal of Rock Mechanics and Mining Sciences & Geomechanics Abstracts 28, 451-456.

Zanetti, A., Mazzucchelli, M., Rivalenti, G., Vannucci, R., 1999. The Finero phlogopite-peridotite massif: an example of subduction-related metasomatism. Contrib Mineral Petrol 134, 107-122.

Zingg, A., 1983. The Ivrea and Strona-Ceneri zones (Southern Alps, Ticino and N-Italy) - A review. Schweizerische mineralogische und petrographische Mitteilungen 63, 361-392.

Appendix: Definition of magnetic and seismic tensors

Matlab code defining magnetic and seismic single crystal properties is given below:

```
%% definition of coordinate systems for magnetic properties
cs_hbl= crystalSymmetry('2/m',[ 9.803 18.046 5.313],[ 90, 105.05, 90
]*degree,'x||a*','z||c', 'mineral','hornblende');
cs_en = crystalSymmetry('mmm',[ 18.2457  8.7984  5.1959],[  90.,
90.0,90.]*degree,'x||a','z||c','mineral','enstatite');
cs_cpx = crystalSymmetry('2/m',[9.7456,8.9198,5.2516],[90.0,105.86,
90.0]*degree,'x||a*','z||c','mineral','clinopyroxene');
cs_ol = crystalSymmetry('mmm',[  4.8195, 10.4788,  6.0873], [  90.0, 90.0,
90.0,]*degree,'x||a','z||c','mineral','olivine');
cs_mica = crystalSymmetry('2/m',[  5.308  9.190 10.155],[  90.00, 100.08,
90.00]*degree,'x||a','z||c*','mineral','phlogopite');

%% single crystal magnetic properties
% olivine
k1_ol = 1.6668e-7;
k2_ol = 1.5794e-7;
k3_ol = 1.5566e-7;
susc_ol = [k2_ol 0 0; 0 k3_ol 0; 0 0 k1_ol];
C_ol = tensor(susc_ol, cs_ol)

% enstatite
k1_en = 1.9393e-7;
k2_en = 1.8078e-7;
k3_en = 1.7526e-7;
susc_en = [k2_en 0 0; 0 k3_en 0; 0 0 k1_en];
C_en = tensor(susc_en, cs_en)

% hornblende
k1_hbl = 2.0439e-7;
k2_hbl = 2.0140e-7;
k3_hbl = 1.7789e-7;
susc_hbl = [k3_hbl 0 0; 0 k1_hbl 0; 0 0 k2_hbl];
C_hbl = tensor(susc_hbl, cs_hbl)

% diopside
k1_cpx = 3.6816e-8;
k2_cpx = 3.6021e-8;
k3_cpx = 3.2197e-8;
susc_cpx = [(k1_cpx+k3_cpx)/2 0 (k1_cpx-k3_cpx)/2; 0 k2_cpx 0; (k1_cpx-
k3_cpx)/2 0 (k1_cpx+k3_cpx)/2];
C_cpx = tensor(susc_cpx, cs_cpx)

% mica
k1_mica = 1.3634E-07;
k3_mica = 1.1390E-07;
susc_mica = [k1_mica 0 0; 0 k1_mica 0; 0 0 k3_mica];
C_mica = tensor(susc_mica, cs_mica)
```

```
%% single crystal elastic properties
% clinopyroxene
rho_cpx= 3.2860;
cs_cpx = crystalSymmetry('2/m',[  9.7456  8.9198  5.2516],...
 [  90.0000 105.8600  90.0000]*degree,'x||a*','z||c',...
 'mineral','clinopyroxene');
M_cpx =....
 [[  228.10   78.80   70.20    0.00    7.90    0.00];...
 [    78.80  181.10   61.10    0.00    5.90    0.00];...
 [    70.20   61.10  245.40    0.00   39.70    0.00];...
 [     0.00    0.00    0.00   78.90    0.00    6.40];...
 [     7.90    5.90   39.70    0.00   68.20    0.00];...
 [     0.00    0.00    0.00    6.40    0.00   78.10]];
S_cpx = tensor(M_cpx,cs_cpx);

% enstatite
 rho_en = 3.3060;
cs_en = crystalSymmetry('mmm',[ 18.2457  8.7984  5.1959],...
 [  90.0000  90.0000  90.0000]*degree,'x||a','z||c',...
 'mineral','enstatite');
M_en =....
 [[  236.90   79.60   63.20    0.00    0.00    0.00];...
 [    79.60  180.50   56.80    0.00    0.00    0.00];...
 [    63.20   56.80  230.40    0.00    0.00    0.00];...
 [     0.00    0.00    0.00   84.30    0.00    0.00];...
 [     0.00    0.00    0.00    0.00   79.40    0.00];...
 [     0.00    0.00    0.00    0.00    0.00   80.10]];
S_en = tensor(M_en,cs_en);

% olivine
rho_ol= 3.221;
cs_ol = crystalSymmetry('mmm',[  4.8195 10.4788  6.0873],...
 [  90.0000  90.0000  90.0000]*degree,'x||a','z||c',...
 'mineral','olivine');
M_ol =....
 [[  328.00   69.00   69.00    0.00    0.00    0.00];...
 [    69.00  200.00   73.00    0.00    0.00    0.00];...
 [    69.00   73.00  235.00    0.00    0.00    0.00];...
 [     0.00    0.00    0.00   66.70    0.00    0.00];...
 [     0.00    0.00    0.00    0.00   81.30    0.00];...
 [     0.00    0.00    0.00    0.00    0.00   80.90]];
S_ol = tensor(M_ol,cs_ol);

% hornblende
 rho_hbl= 3.163;
cs_hbl = crystalSymmetry('2/m',[ 9.803 18.046 5.313],...
 [ 90, 105.05, 90 ]*degree,'x||a*','z||c',...
 'mineral','hornblende');
 M_hbl =....
 [[  141.60   57.10   49.60    0.00   -0.20    0.00];...
 [    57.10  197.80   60.90    0.00  -10.90    0.00];...
 [    49.60   60.90  225.40    0.00  -31.40    0.00];...
 [     0.00    0.00    0.00   75.80    0.00    3.30];...
 [    -0.20  -10.90  -31.40    0.00   49.90    0.00];...
 [     0.00    0.00    0.00    3.30    0.00    51.7]];
S_hbl = tensor(M_hbl,cs_hbl);

% mica
rho_mica= 2.872;
cs_mica = crystalSymmetry('2/m',[  5.308  9.190 10.155],...
 [  90.00 100.08  90.00]*degree,'x||a','z||c*',...
```

```
 'mineral','phlogopite');
M_mica =....
 [[  181.00   48.00   12.00    0.00  -16.00    0.00];...
 [    48.00  185.00   12.00    0.00   -5.00    0.00];...
 [    12.00   12.00   62.00    0.00   -1.00    0.00];...
 [     0.00    0.00    0.00   14.00    0.00   -6.00];...
 [   -16.00   -5.00   -1.00    0.00   20.00    0.00];...
 [     0.00    0.00    0.00   -6.00    0.00   68.00]];
S_mica = tensor(M_mica,cs_mica);
```

Figures and Tables

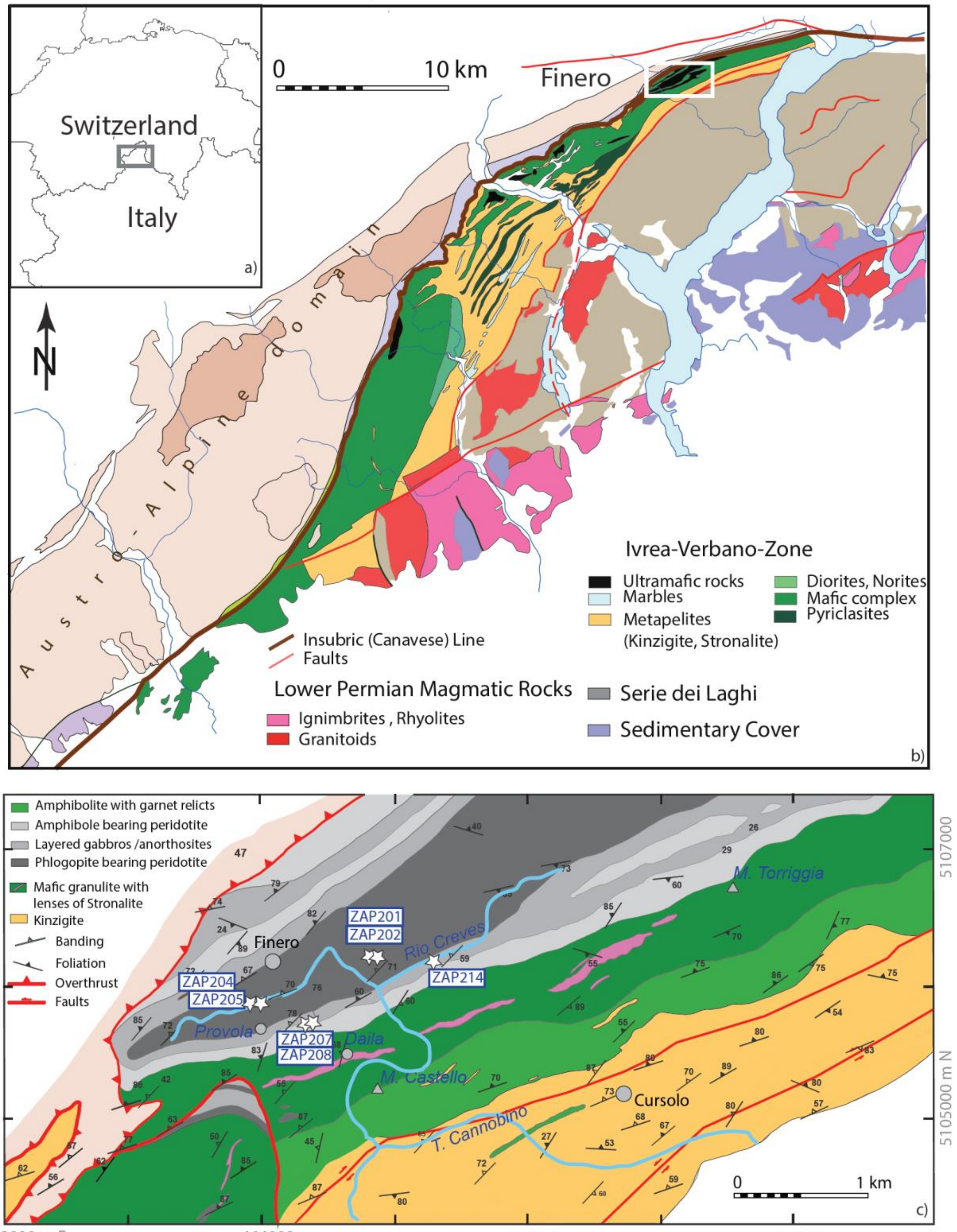

Figure 1: (a) Geographical location of the studied area; (b) Geological sketch of the Ivrea Verbano Zone in the westernmost Southern Alps and of the tectonic units of the Southern and Western Alps (modified after Brack et al., 2010); (c) Sample locations and simplified geological map of the ultramafic body in the Finero area, and its country rocks in the sampled area. Geographic coordinates in WGS84/UTM zone 32N.

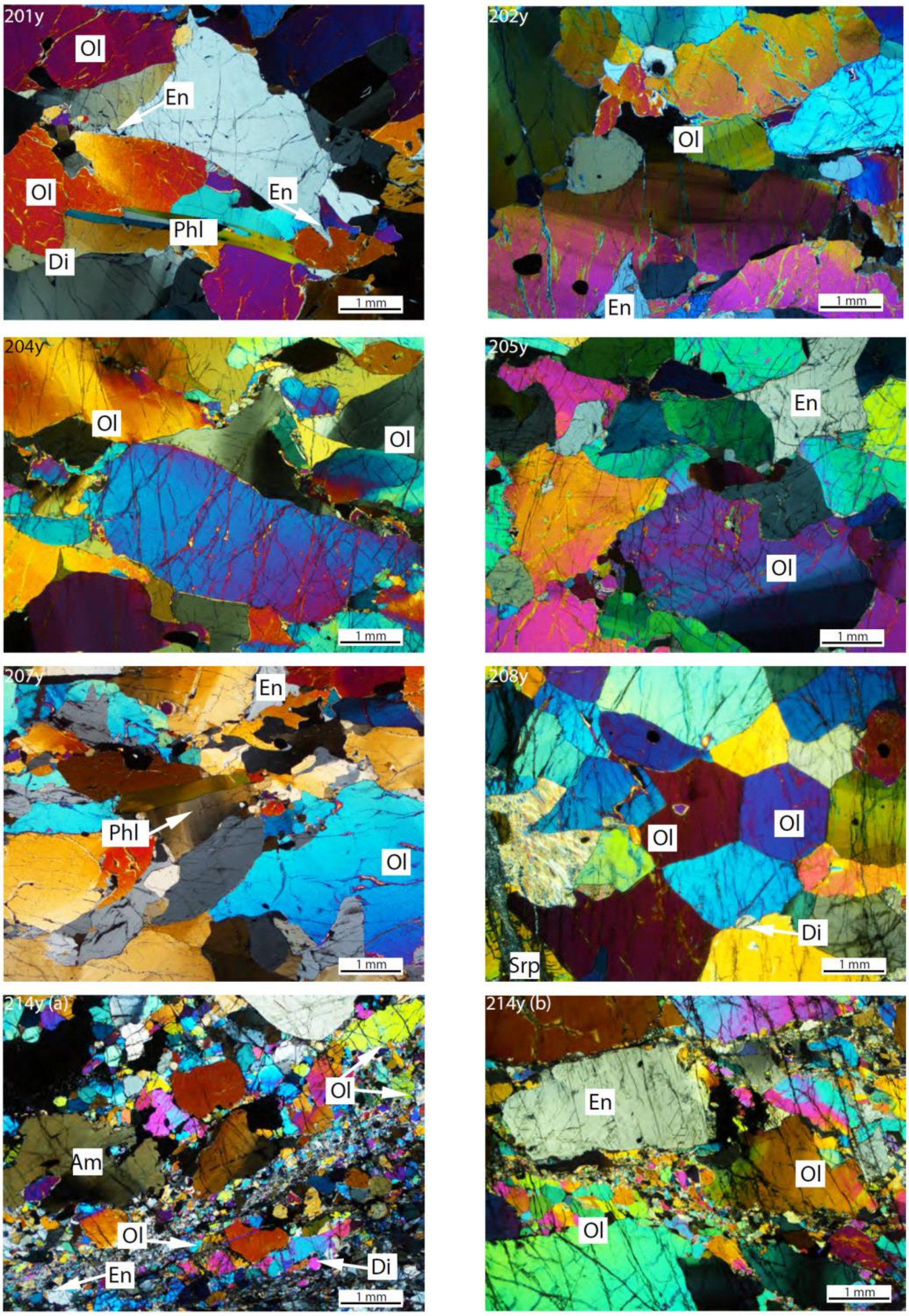

Figure 2: Microstructures under optical microscope (cross-polarized light) of each analyzed sample group. Sample names indicated at top left corner. Samples ZAP201, ZAP202, ZAP204, ZAP205 and ZAP207 are harzburgites, ZAP208 a dunite, and ZAP214 a harzburgite with protomylonitic texture. Note the following details of the microstructures: for olivine: Shape preferred orientation (ZAP201y to 207y), polygonal shape (ZAP208y), core-mantle structure (ZAP214a, b), sub-grain boundaries (ZAP204y, ZAP205y); for enstatite: irregular shape and pinnacle termination (arrows in ZAP201y); for phlogopite: pinning of olivine grain boundaries at the contact with phlogopite. Minerals: Ol – olivine, En – enstatite, Di – diopside, Phl – phlogopite, Am – amphibole, Srp serpentine.

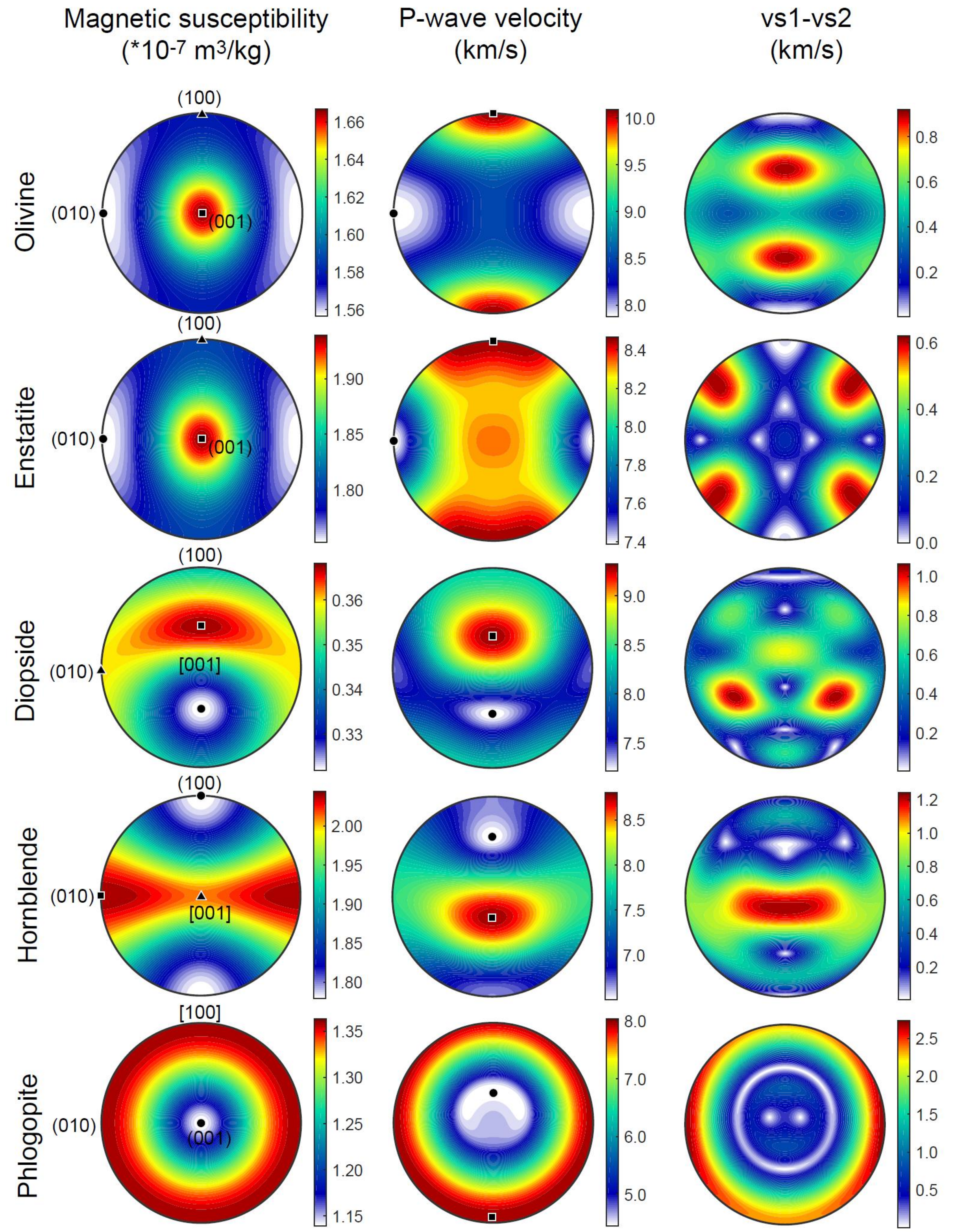

Figure 3: Single crystal magnetic and seismic properties in a crystallographic reference frame. Principal directions (black squares, triangles and circles) are indicated for magnetic tensors, and minima and maxima (black circles and squares) for compressional wave velocities.

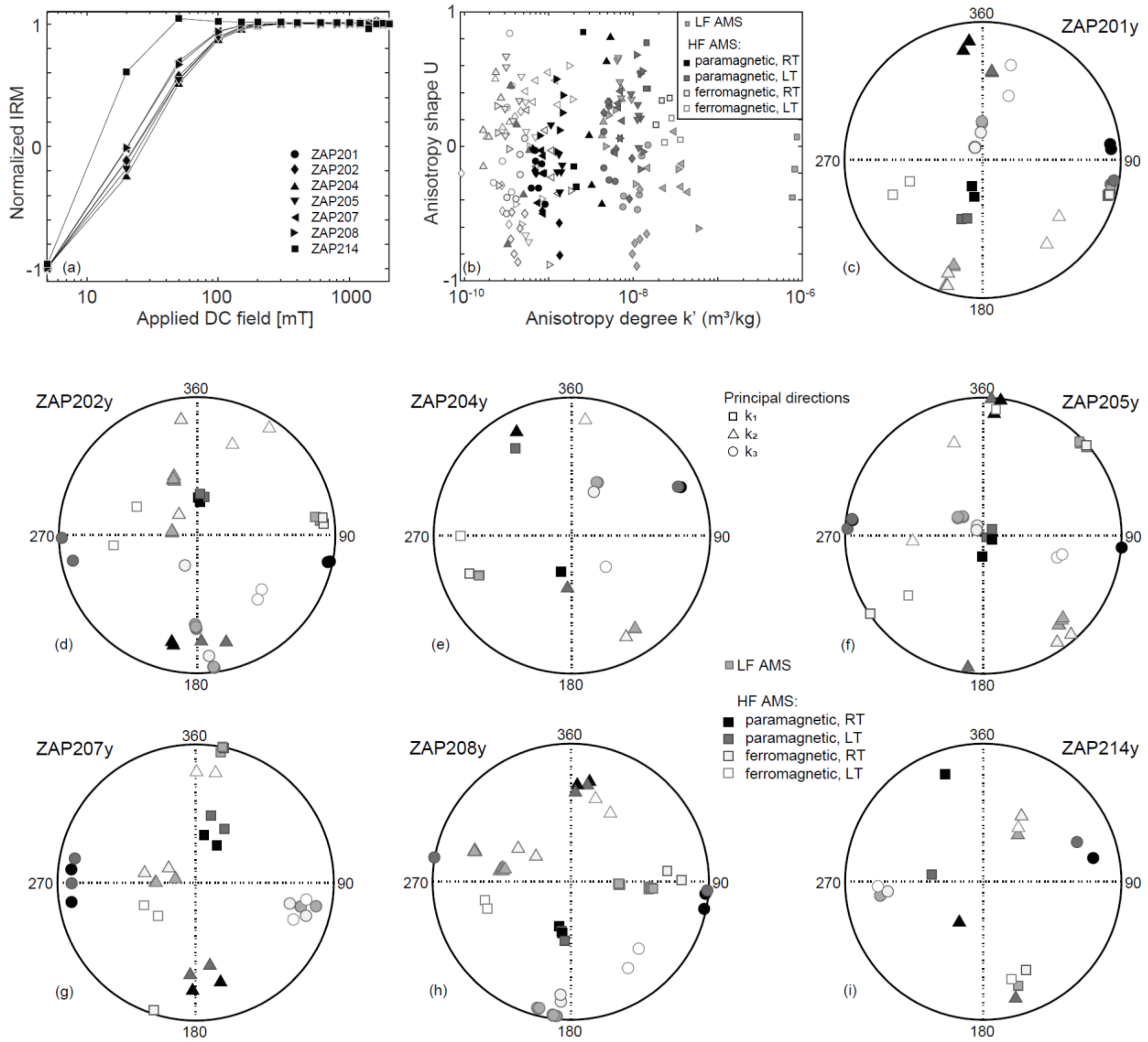

Figure 4: Magnetic results. (a) Isothermal remanent magnetization (IRM) acquisition, showing that low-coercivity grains such as magnetite dominate the ferromagnetic grains. (b) Overview of anisotropy degree and shape measured in different field and temperature conditions. (c-i) Comparison of low-field AMS to the paramagnetic and ferromagnetic components isolated from high-field AMS for the y-cores of each site. RT and LT refer to room temperature and 77 K, respectively, at which high-field experiments were performed. Repeat measurements of low-field AMS show good reproducibility of directional data.

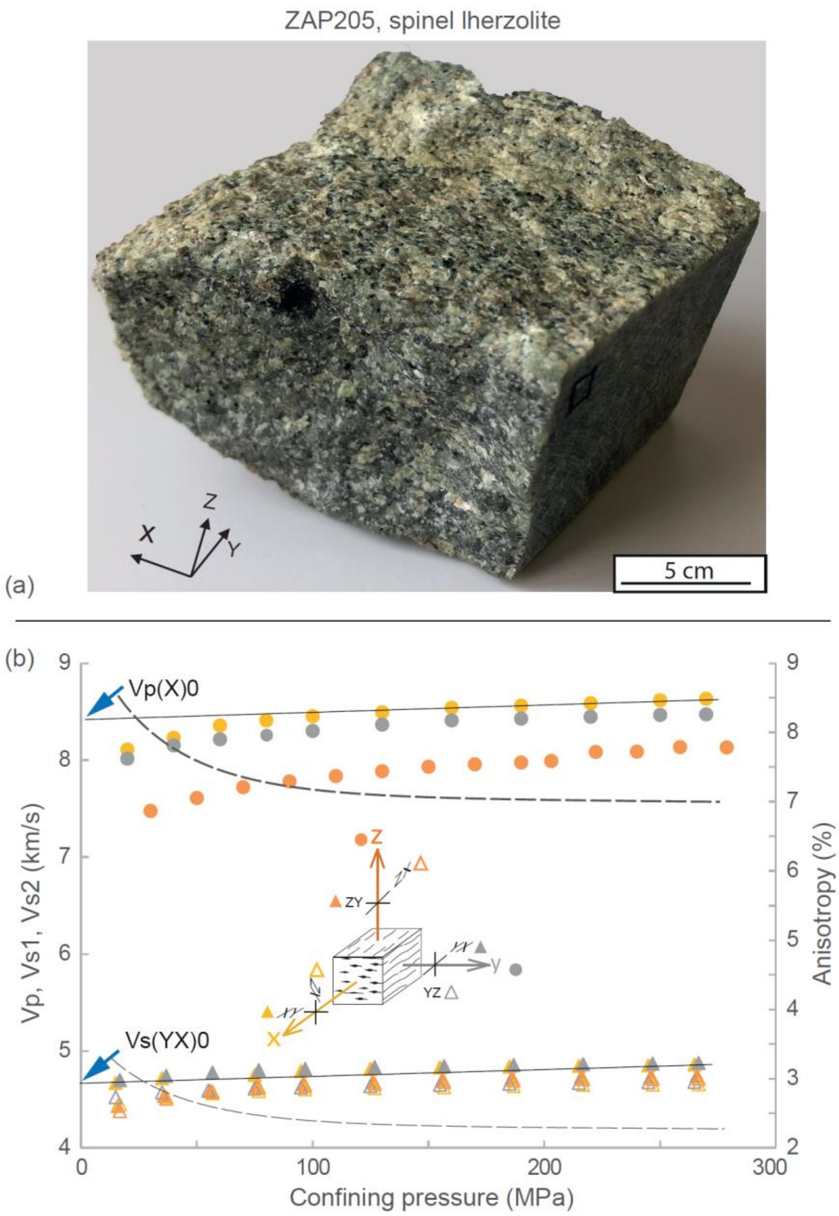

Figure 5: Effect of pressure at room temperature on P-wave (Vp) and S-wave (Vs) velocities on a representative lherzolite sample, ZAP205. Velocities are measured along the three structural directions: X parallel to lineation, Y normal to lineation and parallel to foliation, and Z normal to foliation (inset). Six shear-wave velocities were measured, using shear-wave notation similar to stress-strain notation: the first index indicates the direction of particle motion, and the second indicates the plane of wave propagation. For each direction, the linear regression of the velocity/pressure curve above 100 MPa is used to calculate a set of reference values of velocity at 0 pressure; here only the compressional wave along X and the shear wave propagating along X in the foliation plane (XY) are shown. Elastic wave velocities are fit to the empirical formula proposed by Wepfer and Christensen (1991), relating velocity to confining pressure, and anisotropy for P and S waves (dashed line, thick and thin respectively) is then calculated from the fitting curves, as explained in the text.

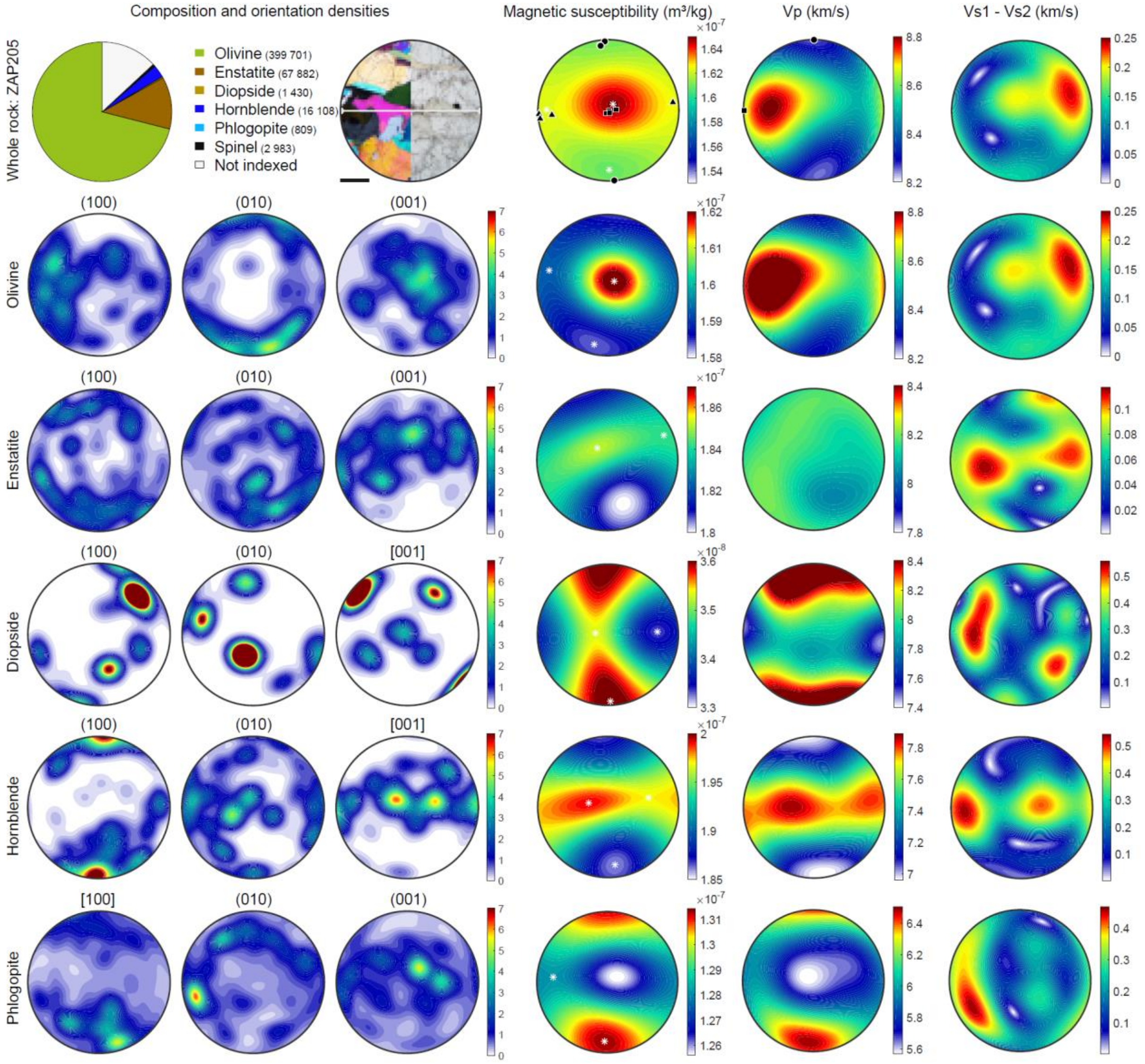

Figure 6: Orientation density functions and modeled and measured magnetic and seismic anisotropies for sample ZAP205. Modal composition determined from EBSD data; numbers in brackets indicate the measurements for each phase. All data shown in a coordinate system defined by the sample's macroscopic foliation and lineation (indicated in white grey on the thin section photograph). Scale bar 1 mm. Orientation density functions measured on a regularly spaced grid, and shown as multiples of uniform distribution (color scale). Modeled physical properties (color scale) and principal directions for the magnetic tensor (white asterisk) for each phase and the entire rock are shown in addition to measurements for magnetic and P-wave anisotropy (black symbols, where square, triangle and circle indicate the maximum, intermediate and minimum principal axes, respectively) on the rock samples. Cf the online supplementary for similar figures for the other samples.

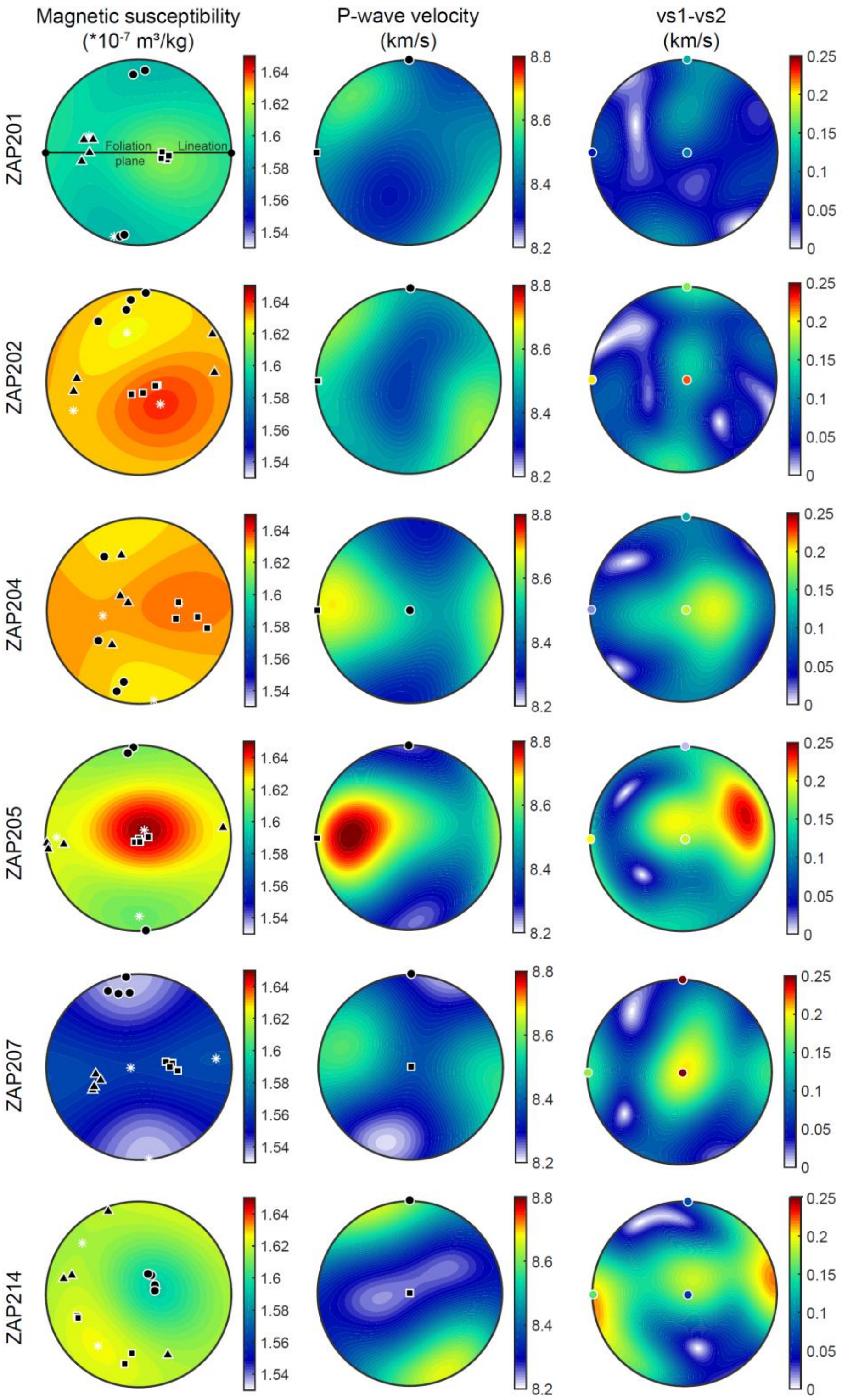

Figure 7: Comparison between modeled (color scale) and measured (symbols) principal directions of magnetic and seismic anisotropies. For magnetic properties, squares, triangles and circles define the maximum, intermediate and minimum principal susceptibilities respectively, and white asterisk indicate the principal directions of the modeled tensors. Measured maximum and minimum P-wave velocities are indicated by squares and circles, respectively. Circles on the vs1-vs2 plot indicate the measured differences between vs1 and vs2 using the same color scale as the models.

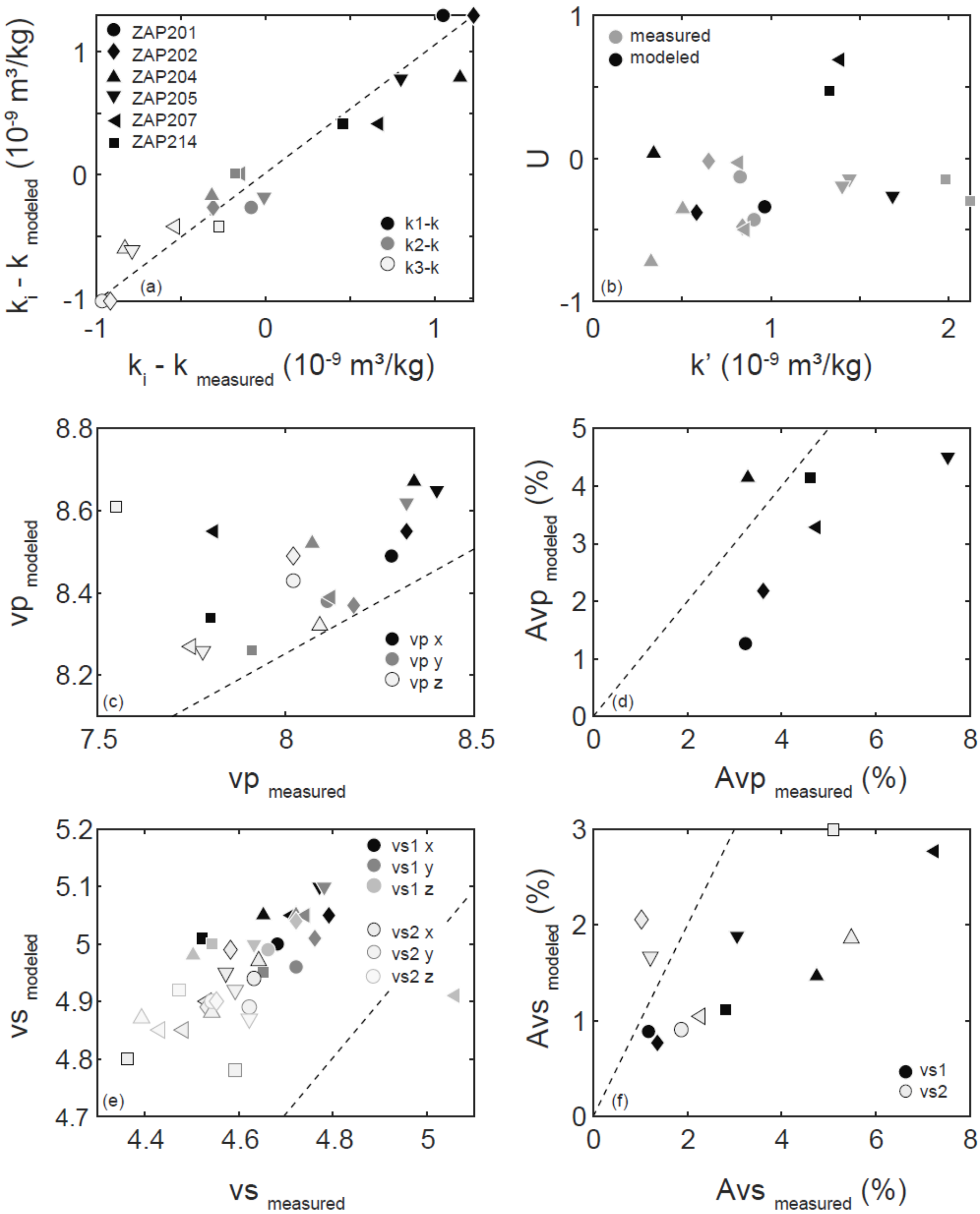

Figure 8: Comparison of modeled and measured anisotropy parameters for magnetic susceptibility (a,b), P-waves (c,d) and S-waves (e,f). Dashed lines indicate equal values for measurement and model.

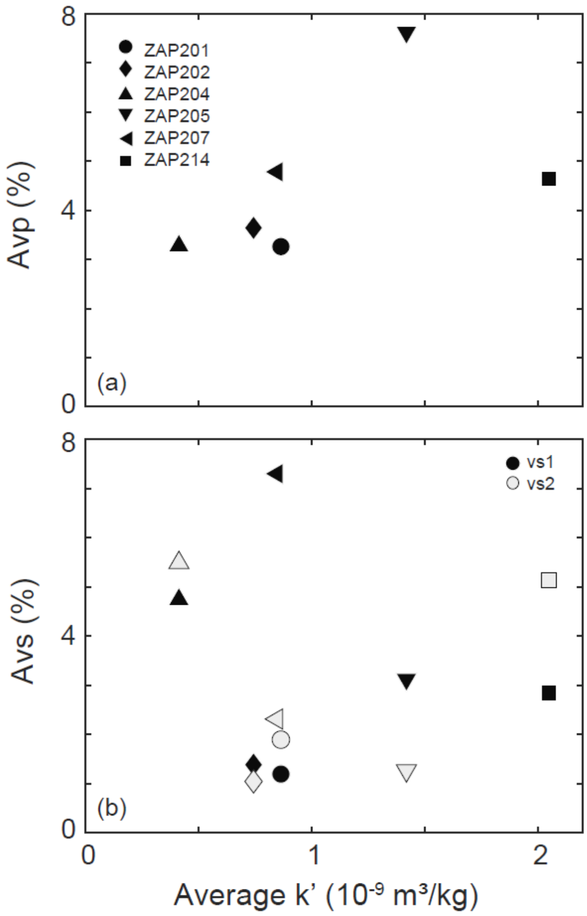

Figure 9: Relationship between measured magnetic and seismic degree of anisotropy for P-waves (a) and S-waves (b,c). For the magnetic anisotropy the average of the 2 measured specimens cut from the longer core for seismic measurements is shown.

Table 1: Modal compositions (volume %) of the samples determined by (a) point count analysis with petrographic optical microscope (cf. Hefferan and O'Brien, 2010 for a description of the method), and (b) SEM (EDS and EBSD) analyses:

a) Modal composition from optical microscopy

	ZAP201	ZAP202	ZAP204	ZAP205	ZAP207	ZAP208	ZAP214
Olivine	70	70	76	70	70	80	65
Enstatite	9	15	13	13	10	9	10
Diopside	15	10	3	8	10	10	0
Hornblende	0	0	6	0	0	0	20
Phlogopite	5	3	1	8	3	0	0
Serpentine	0	0	0	0	1	0	2
Spinel	1	2	1	1	6	1	3

b) Modal composition from SEM

	ZAP201x1	ZAP202z2	ZAP204x2	ZAP205y2	ZAP207z1	ZAP208x1	ZAP214x2
Olivine	75	70	76	71	56	*	64
Enstatite	18	11	19	12	25	*	7
Diopside	2	1	0	0	8	*	1
Hornblende	3	2	4	3	9	*	24
Phlogopite	1	0	0	0	0	*	0
Spinel	1	1	1	1	0	*	1
Not indexed	1	15	1	13	2	*	4

* ZAP208x1 is coarse-grained, so that the EBSD data is not statistically representative

Table 2: Bulk density, grain density, effective porosity and seismic measurements. Seismic velocities are given as P- and S-wave speeds (Vs01 and Vs02 denoting the two perpendicular particle motions for S-waves) extrapolated to 0 pressure, and their pressure derivatives. For P-waves, the anisotropy A(%) was calculated using the average of the three measurements as mean velocity.

Sample	Bulk density (g/cm^3)	core	Grain density (g/cm^3)	Porosity (%)	Vp0 (km/s)	Pressure derivative ($m{\cdot}s^{-1}/MPa$)	Anisotropy Avp (%)	$Vs0_1$ (km/s)	Pressure derivative ($m{\cdot}s^{-1}/MPa$)	$Vs0_2$ (km/s)	Pressure derivative ($m{\cdot}s^{-1}/MPa$)	Anisotropy Avs_1 (%)	Anisotropy Avs_2 (%)	$Vs0_1$ - $Vs0_2$ (m/s)	Average
ZAP201	3.27		3.28	0.22											
		x			8.28	0.39		4.68	0.28	4.63	0.20			55	
		y			8.11	0.40		4.72	0.15	4.62	0.20			96	
		z			8.02	0.44	3.26	4.66	0.19	4.54	0.24	1.19	1.89	120	90
ZAP202	3.29		3.29	0.19											
		x			8.32	0.47		4.79	0.29	4.58	0.44			205	
		y			8.18	0.49		4.76	0.35	4.53	0.37			222	
		z			8.02	0.58	3.64	4.72	0.33	4.55	0.35	1.38	1.04	167	198
ZAP204	3.26		3.27	0.13											
		x			8.34	0.30		4.65	0.39	4.64	0.22			17	
		y			8.07	0.34		4.72	0.29	4.54	0.23			186	
		z			8.09	0.45	3.31	4.50	0.30	4.39	0.24	4.78	5.52	117	107
ZAP205	3.28		3.28	0.20											
		x			8.40	0.87		4.77	0.26	4.57	0.28			207	
		y			8.32	0.58		4.78	0.30	4.59	0.27			187	
		z			7.78	1.04	7.58	4.63	0.34	4.62	0.31	3.08	1.23	12	135
ZAP207	3.26		3.26	0.09											
		x			7.81	0.44		4.71	0.32	4.53	0.28			173	
		y			8.12	0.40		4.74	0.22	4.48	0.25			257	
		z			7.75	0.52	4.78	5.06	0.33	4.43	0.23	7.30	2.31	630	353
ZAP208	3.23		3.23	0.19											
		x			7.89	0.60									
		y			7.48	0.90		Not measured							
		z			7.47	0.70	5.44								
ZAP214	3.34		3.34	0.03											
		x			7.80	0.02		4.52	0.64	4.36	0.69			160	
		y			7.91	0.28		4.65	0.38	4.59	0.36			60	
		z			7.55	0.41	4.64	4.54	0.46	4.47	0.76	2.84	5.14	70	97

Table 3: Comparison of measured and modeled data for magnetic and seismic properties. Magnetic data is represented as deviatoric principal susceptibilities, the degree (k') and shape (U) of the anisotropy, and seismic data is shown as P- and S-wave velocities parallel to the 3 structural directions, as well as anisotropy degree A(%) for Vp0.

Magnetic anisotropy							
		Mean susceptibi	**Principal susceptibilities**			**Anisotropy parameters**	
Sample		**k (m3/kg)**	**k1-k (m3/kg)**	**k2-k (m3/kg)**	**k3-k (m3/kg)**	**k' (m3/kg)**	**U**
ZAP201x	Model	1.60E-07	1.29E-09	-2.66E-10	-1.03E-09	9.64E-10	-0.34
ZAP201x1	Measurement		1.05E-09	-8.52E-11	-9.67E-10	8.26E-10	-0.13
ZAP201x2	Measurement		1.23E-09	-3.10E-10	-9.18E-10	9.04E-10	-0.43
ZAP202z	Model	1.63E-07	7.83E-10	-1.76E-10	-6.07E-10	5.81E-10	-0.38
ZAP202z1	Measurement		1.15E-09	-3.18E-10	-8.32E-10	8.39E-10	-0.48
ZAP202z2	Measurement		8.00E-10	-9.36E-12	-7.90E-10	6.49E-10	-0.02
ZAP204x	Model	1.63E-07	4.12E-10	7.88E-12	-4.20E-10	3.40E-10	0.03
ZAP204x1	Measurement		6.74E-10	-1.43E-10	-5.31E-10	5.03E-10	-0.36
ZAP204x2	Measurement		4.57E-10	-1.79E-10	-2.76E-10	3.25E-10	-0.73
ZAP205x	Model	1.63E-07	2.22E-09	-3.54E-10	-1.86E-09	1.68E-09	-0.26
ZAP205x1	Measurement		1.84E-09	-1.69E-10	-1.68E-09	1.44E-09	-0.14
ZAP205x2	Measurement		1.82E-09	-2.15E-10	-1.60E-09	1.40E-09	-0.19
ZAP207z	Model	1.55E-07	1.22E-09	7.32E-10	-1.95E-09	1.39E-09	0.69
ZAP207z1	Measurement		1.18E-09	-3.34E-10	-8.44E-10	8.58E-10	-0.50
ZAP207z2	Measurement		1.02E-09	-1.84E-11	-9.98E-10	8.22E-10	-0.03
ZAP214x	Model	1.61E-07	1.33E-09	4.88E-10	-1.81E-09	1.33E-09	0.47
ZAP214x1	Measurement		2.82E-09	-5.19E-10	-2.30E-09	2.12E-09	-0.30
ZAP214x2	Measurement		2.54E-09	-2.47E-10	-2.29E-09	1.98E-09	-0.15

Seismic anisotropy						
		Density	**P-wave velocities**			**Anisotropy parameter**
Sample		**rho_tot (g/cm3)**	**vpx (km/s)**	**vpy (km/s)**	**vpz (km/s)**	**A vp %**
ZAP201x	Model	3.23	8.49	8.38	8.43	1.29
ZAP201	Measurement		8.28	8.11	8.02	3.26
ZAP202z	Model	3.23	8.55	8.37	8.49	2.21
ZAP202	Measurement		8.32	8.18	8.02	3.64
ZAP204x	Model	3.21	8.67	8.52	8.32	4.18
ZAP204	Measurement		8.34	8.07	8.09	3.31
ZAP205x	Model	3.20	8.65	8.62	8.26	4.55
ZAP205	Measurement		8.40	8.32	7.78	7.58
ZAP207z	Model	3.17	8.55	8.39	8.27	3.32
ZAP207	Measurement		7.81	8.12	7.75	4.78
ZAP214x	Model	3.10	8.34	8.26	8.61	4.19
ZAP214	Measurement		7.80	7.91	7.55	4.64

		S-wave velocities					
Sample		**vs1x (km/s)**	**vs1y (km/s)**	**vs1z (km/s)**	**vs2x (km/s)**	**vs2y (km/s)**	**vs2z (km/s)**
ZAP201x	Model	5.00	4.96	4.99	4.94	4.89	4.90
ZAP201	Measurement	4.68	4.72	4.66	4.63	4.62	4.54
ZAP202z	Model	5.05	5.01	5.04	4.99	4.89	4.90
ZAP202	Measurement	4.79	4.76	4.72	4.58	4.53	4.55
ZAP204x	Model	5.05	5.05	4.98	4.97	4.88	4.87
ZAP204	Measurement	4.65	4.72	4.50	4.64	4.54	4.39
ZAP205x	Model	5.10	5.10	5.00	4.95	4.92	4.87
ZAP205	Measurement	4.77	4.78	4.63	4.57	4.59	4.62
ZAP207z	Model	5.05	5.05	4.91	4.90	4.85	4.85
ZAP207	Measurement	4.71	4.74	5.06	4.53	4.48	4.43
ZAP214x	Model	5.01	4.95	5.00	4.80	4.78	4.92
ZAP214	Measurement	4.52	4.65	4.54	4.36	4.59	4.47